

# Derivation of 1.064 $\mu\text{m}$ albedo on the C-type asteroid Ryugu from laser pulse intensity measurement of the Hayabusa2 LIDAR

Ryuhei Yamada (✉ [ryamada@u-aizu.ac.jp](mailto:ryamada@u-aizu.ac.jp))

The University of Aizu: Aizu Daigaku <https://orcid.org/0000-0002-0074-3256>

**Keiko Yamamoto**

National Astronomical Observatory of Japan

**Shoko Oshigami**

Japan Aerospace Exploration Agency

**Hiroshi Araki**

National Astronomical Observatory of Japan

**Hiroki Senshu**

Chiba Institute of Technology: Chiba Kogyo Daigaku

**Hiroto Noda**

National Astronomical Observatory of Japan

**Noriyuki Namiki**

National Astronomical Observatory of Japan

**Koji Matsumoto**

National Astronomical Observatory of Japan

**Fumi Yoshida**

University of Occupational and Environmental Health Japan: Sangyo Ika Daigaku

**Shinsuke Abe**

Nihon University: Nihon Daigaku

**Naru Hirata**

The University of Aizu: Aizu Daigaku

**Sho Sasaki**

Osaka University: Osaka Daigaku

**Takahide Mizuno**

Japan Aerospace Exploration Agency

---

**Full paper**

**Keywords:** C-type asteroid, albedo, LIDAR, Hayabusa2

**Posted Date:** April 12th, 2022

**DOI:** <https://doi.org/10.21203/rs.3.rs-1430788/v1>

**License:**  This work is licensed under a Creative Commons Attribution 4.0 International License.

[Read Full License](#)

---

1 **Title page:**

2 **Title: Derivation of 1.064  $\mu\text{m}$  albedo on the C-type asteroid Ryugu from laser**  
3 **pulse intensity measurement of the Hayabusa2 LIDAR**

4

5 Author #1: Ryuhei Yamada, ryamada@u-aizu.ac.jp

6 Author #2: Keiko Yamamoto, keiko.yamamoto@nao.ac.jp

7 Author #3: Shoko Oshigami, oshigami.shohko@jaxa.jp

8 Author #4: Hiroshi Araki, araki.hiroshi@nao.ac.jp

9 Author #5: Hiroki Senshu, senshu@perc.it-chiba.ac.jp

10 Author #6: Hirotomo Noda, hirotomo.noda@nao.ac.jp

11 Author #7: Noriyuki Namiki, nori.namiki@nao.ac.jp

12 Author #8: Koji Matsumoto, koji.matsumoto@nao.ac.jp

13 Author #9: Fumi Yoshida, fumi-yoshida@med.uoeh-u.ac.jp

14 Author #10: Shinsuke Abe, shinsuke.avell@gmail.com

15 Author #11: Naru Hirata, naru@u-aizu.ac.jp

16 Author #12: Sho Sasaki, sasaki.sho.sci@osaka-u.ac.jp

17 Author #13: Takahide Mizuno, mizuno.takahide@jaxa.jp

18

19 Institutional addresses of each author are listed in [Author's information].

20

21 **Indicate the corresponding author**

22 Author #1: Ryuhei Yamada, The University of Aizu, Tsuruga, Ikki-machi, Aizu-

23 Wakamatsu, Fukushima 965-8580, Japan, ryamada@u-aizu.ac.jp

24

25 (go to new page)

26

27 **Abstract**

28 Japanese asteroid explorer Hayabusa2 arrived at C-type asteroid 162173 Ryugu in June  
29 2018. Laser altimeter (LIDAR) onboard Hayabusa2 measured its own transmitted laser  
30 pulse intensity and returned pulse intensity from the surface of Ryugu until November  
31 2019. Because the Ryugu surface is extremely rough, topography dominates material  
32 property in the conventional derivation of normal albedo. We develop a method to  
33 derive the albedo from the rough surface of the C-type asteroid at the LIDAR laser  
34 wavelength of 1.064  $\mu\text{m}$ . Using the intensity data obtained before the conjunction of the  
35 spacecraft with the Sun, the albedo map covering an equatorial band between  $-40^\circ$  and  
36  $+20^\circ$  in the latitude is created with  $2^\circ$  by  $2^\circ$  resolution. The average of the albedo is  
37  $0.0406 \pm 0.0031$ , while about half of them are in the range between 0.04 and 0.045.  
38 The low and uniform albedo feature is common to other remote-sensing observations of  
39 Ryugu by visible and near-infrared cameras onboard the Hayabusa2.

40

41

42

## 43 **Keywords**

44 C-type asteroid, albedo, LIDAR, Hayabusa2

45

## 46 **Main Text**

### 47 **1. Introduction**

48

49 In June 2018, the Japanese asteroid explorer Hayabusa2 arrived at C-type asteroid  
50 (162173) Ryugu after cruising for about three and half years. Ryugu is one of the near-  
51 Earth asteroids. Our knowledge of space weathering on the surface of C-type asteroids,  
52 which contain carbon, organic matter, and water metamorphic minerals, is still limited.  
53 The survey of surface albedo distribution by Hayabusa2 is a unique opportunity to collect  
54 information on space weathering of C-type asteroids. In addition to space weathering,  
55 three mechanisms are considered as causes of albedo variations on the asteroid surface:  
56 the land sliding due to tidal effects (Binzel et al., 2010), aqueous alteration (Vilas, 2008;  
57 Sugita et al., 2013), and adherence of the material from other bodies (Reddy et al., 2012).  
58 The Hayabusa2 has four scientific optical instruments: optical navigation camera (ONC),

59 near-infrared spectrometer (NIRS3), thermal infrared imager (TIR), and laser altimeter  
60 (LIDAR). Sugita et al. (2019) conducted the first global albedo analysis of Ryugu using  
61 the ONC images. They reported that the asteroid has relatively uniform surface  
62 reflectance. The geometric albedo is  $0.045 \pm 0.002$  at  $0.55 \mu\text{m}$ , similar to the darkest  
63 asteroids (235) Mathilde and other Cb-type asteroids (e.g., Bus et al., 2002). Ryugu's  
64 spectral feature between  $0.4$  and  $0.9 \mu\text{m}$  is observed by ONC, indicating no  $0.7 \mu\text{m}$   
65 absorption band and little spectral variation. Because of these properties, Ryugu is  
66 classified as a Cb-type overall, among C-type. However, boulders exhibit a variety of  
67 color characteristics (Tatsumi et al., 2021). The global observation of Ryugu by NIRS3  
68 has also revealed its low reflectance of  $0.017 \pm 0.002$  at  $2.0 \mu\text{m}$  (Kitazato et al., 2019).  
69 Reflectance in visible ( $0.4 - 0.9 \mu\text{m}$ ) and near-infrared ( $1.8-3.2 \mu\text{m}$ ) indicates that the  
70 surface of Ryugu is compositionally homogeneous and the albedo is very low like  
71 thermally and/or shock-metamorphosed carbonaceous chondrite (Sugita et al., 2019).

72

73 LIDAR's survey with the laser wavelength of  $1.064 \mu\text{m}$  can fill the gap between the  
74 ONC and NIRS3 observation. Generally, the spectral feature around  $1.064 \mu\text{m}$  is an

75 indicator of the olivine or pyroxene. Those are the main components of planetary silicate  
76 materials, which enable the classification of target materials into meteorite types and the  
77 study of the surface evolution of asteroids. For this reason, the near-infrared spectrum  
78 around 1  $\mu\text{m}$  had been measured in the first Hayabusa mission and showed that the  
79 asteroid Itokawa was akin to ordinary chondrite (Kitazato et al., 2008). In addition, the  
80 albedo measurement of Itokawa by LIDAR was attempted during the first Hayabusa  
81 mission (Abe et al., 2006; Mukai et al., 2007). However, the results were inaccurate  
82 because the former LIDAR could not simultaneously record the intensities of the  
83 transmitted and the received pulses.

84

85 Hayabusa2 LIDAR records both transmitted intensity and corresponding returned pulse  
86 intensity for every laser shot. Thus we can calculate in principle the albedo by comparing  
87 transmitted and returned laser energy at 1.064  $\mu\text{m}$ . The albedo measurement by the  
88 LIDAR has three characteristics; (1) the active measurement is employed using a well-  
89 calibrated light source, unlike other passive sensors such as ONC or NIRS3, (2) albedo  
90 data are obtained at a zero-phase angle, and (3) the LIDAR measurement can fill the

91 spectrum gap between ONC and NIRS3.

92

93 A key to the accurate derivation of the surface albedo is precise energy estimation of

94 the returned pulse, which are disturbed by rough asteroid surface. Since the received

95 energy is an integration of the reflected pulse over time and space, detection and response

96 by the LIDAR to the disturbed return are important for the estimation of albedo. As for

97 other planetary bodies, the albedo at 1.064  $\mu\text{m}$  had been measured by the Lunar Orbiter

98 Laser Altimeter (LOLA) on the Moon (Smith et al., 2010) and the Mercury Laser

99 Altimeter (MLA) on the Mercury (Sun et al., 2015). They successfully identified albedo

100 variations in rough polar regions of the Moon and Mercury (e.g., Zuber et al., 2012;

101 Neumann et al., 2013). The LOLA and MLA have multiple receiving telescopes, and the

102 receiver can monitor the returned laser pulse energies and the pulse widths above a

103 threshold. These functions help estimate the shapes and energies of the returned pulses

104 accurately.

105

106 The OSIRIS-REx Laser Altimeter (OLA) constructed the shape model of Bennue,

107 which is another C-type asteroid similar to Ryugu, from laser ranging data (Barnouin et  
108 al., 2020). The preliminary albedo analysis was conducted using the return intensity count  
109 (Neumann et al., 2020). The OLA has two types of laser transmitters of different energies  
110 and can scan a field over  $10^\circ$  by  $10^\circ$  using a scanning mirror with a maximum sampling  
111 rate of 10 kHz (Daly et al., 2017; Barnouin et al., 2020). On the other hand, the Hayabusa2  
112 LIDAR has only NEAR and FAR receiving telescopes. One fixed laser transmitter obtain  
113 8-bit digital values of the transmitted and received pulse energies with a maximum  
114 sampling rate of 1 Hz. Unlike other planetary laser altimeter, pulse shapes are not  
115 measured. Such hardware design is suitable for small and middle-class planetary  
116 explorations whose resources are severely limited. Therefore, the first objective of this  
117 paper is to establish a method to calculate the albedo of the rough surface under the  
118 limitation of the Hayabusa2 LIDAR. The second objective is to provide the map of 1.064  
119  $\mu\text{m}$  albedo distribution on the C-type asteroid Ryugu.

120

121 The contents of this paper are as follows; in Chapter 2, we review the specification and  
122 data acquisition of the Hayabusa2 LIDAR. In Chapter 3, a method to derive the albedo

123 based on the return pulse simulation and the ground experimental results is explained.  
124 Also, the correction of periodic variation and the remaining errors of the albedo are  
125 discussed. Then, we describe observation by the LIDAR on Ryugu and the data selection  
126 in Chapter 4. Finally, the results of albedo mapping are presented in Chapter 5. We also  
127 discuss the properties of the 1.064  $\mu\text{m}$  albedo distribution, compare our results with the  
128 one derived from ONC images in Chapter 6, and conclude this study in Chapter 7.

129

## 130 **2. Pulse intensity measurement by the Hayabusa2 LIDAR**

131

132 The specification of the Hayabusa2 LIDAR is summarized in Table 1. See Mizuno et al.,  
133 (2017) for further information including the development processes. In this study, we  
134 analyze data taken by the ‘FAR’ telescope only because the data taken by the ‘NEAR’  
135 telescope were not calibrated for the albedo measurement.

136

137 The laser pulses transmitted to the asteroid surface are recorded as 8-bit digital values.

138 We call this record the transmitted pulse intensity,  $D_T$ .  $D_T$  can be converted to

139 transmitted pulse energy  $E_T$ . The functional relationship between  $E_T$  and  $D_T$  has been  
140 already established by Yamada et al. (2017).

141

142 A small fraction of laser pulse reflected at the solid surface becomes an input to the  
143 LIDAR telescope, and the power is detected by the internal avalanche photodiode (APD)  
144 (Figure 3 in Yamada et al. (2017)). The LIDAR detection system sets three grades of the  
145 APD responsivities; high, middle, and low depending on the bias voltage applied to the  
146 APD (Table 1). The voltage output of the APD is processed in the integration and peak-  
147 hold circuits and is recorded as received pulse intensity  $D_R$  which corresponds to the  
148 pulse energy received by the APD,  $E_{obs}$ . Yamada et al. (2017) describe the energy  
149 conversion from  $D_R$  to  $E_{obs}$  in a special case where the return pulse is rectangular and  
150 10-ns wide. In this paper, we generalize this conversion function to deal with variable  
151 reflected waveforms expected for in situ observation.

152

### 153 **3. Derivation of albedo for rough asteroid surface**

154

### 155 3.1 Data processing

156

157 First, we define the albedo,  $\rho$ , by a ratio of energies injected ( $E_T$ ) into and reflected  
158 ( $E_S$ ) from a laser footprint area on the asteroid surface. Note that the energy injected into  
159 the footprint is equivalent to the transmitted energy of the laser pulse. Then, the albedo is  
160 expressed as

161

$$162 \quad \rho = E_S/E_T \quad (1)$$

163

164 where  $E_S$  is the energy of a laser pulse reflected from the solid surface. By this definition,  
165  $\rho$  can be regarded as a Bond albedo within a footprint, and if the surface is flat and  
166 optically diffusive,  $\rho$  is equivalent to a normal albedo.  $E_T$  can be derived from  $D_T$   
167 (Yamada et al., 2017). On the other hand,  $E_S$  is estimated from the received pulse energy  
168 input into the APD,  $E_{obs}$ , such as

169

$$170 \quad E_{obs} = \beta f_{eff} E_S \quad (2)$$

171

172 where  $\beta$  is the transmissivity of the optical system of the receiver (Table 1), and  $f_{eff}$   
173 is an efficiency of the transfer from the surface to the aperture of the telescope, and the  
174 efficiency depends on the energy distributions of the transmitted laser pulse in time and  
175 space, altitude of the spacecraft, the law of reflectance, and optical properties of the  
176 targeted surface. Then, Equation (1) is rewritten as

177

$$178 \quad \rho = E_{obs}/E_{cal} \quad (3)$$

179

180 where  $E_{cal}$  is the energy input to the APD under the assumption that the albedo is unity,  
181 thus

182

$$183 \quad E_{cal} = \beta f_{eff} E_T \quad (4).$$

184

185 The estimation of  $E_{obs}$  is explained in the next section, and the calculation method of

186  $E_{cal}$  is described in Section 3.3.

187

### 188 **3.2. Estimation of $E_{obs}$ from $D_R$**

189

190 To estimate  $E_{obs}$  from  $D_R$ , we need to know the response of the signal processing unit  
191 of LIDAR to various return pulse waveforms. For that purpose, we have carried out an  
192 experiment using the LIDAR-Engineering Model (EM). The experiment consists of three  
193 steps; 1) synthesizing return pulses whose waveforms are either rectangular, gaussian, or  
194 triangular, 2) inputting these laser pulses into the LIDAR-EM and recording  $D_R$  for each  
195 pulse, 3) simultaneously measuring the strength of the laser pulse as voltage signal by an  
196 oscilloscope and integrating over time. The integrated voltage,  $S_v$  is proportional to  
197  $E_{obs}$ . Then, we determine the ratio of  $S_v$  and  $E_{obs}$  using the data taken in a thermal  
198 vacuum experiment.

199

#### 200 3.2.1 Experiment using the LIDAR-EM

201

202 The LIDAR-EM was manufactured to examine the function of the LIDAR-Flight Model

203 even after the launch of Hayabusa2. The laser pulses were synthesized by the laser pulse  
204 generator developed at Chiba Institute of Technology (Senshu et al., 2017), which can  
205 control the laser pulse's time width and peak amplitude from 10 to 2000 ns every 10-ns  
206 step and 256 levels (0-255), respectively. The time profile of the synthesized laser pulse  
207 is detected by the PIN photodiode in the generator and recorded as the voltage signal by  
208 an oscilloscope. The sampling rate of the oscilloscope is  $10^9$  Hz at the highest.  $S_v$  can  
209 be calculated from this record. Figure 1 shows the schematic diagram of our experimental  
210 setup. The designed laser pulse was transmitted into the FAR telescope of the LIDAR-  
211 EM, and the LIDAR-EM itself recorded  $D_R$  with 1 Hz sampling. The recorded  $D_R$  were  
212 sent to the Ground Support Equipment (GSE) as telemetry data. In this experiment, all  
213 data were measured using the low responsivity of the APD (Table 1).

214

215 We examine four types of the input laser pulse. First, the rectangular pulse is tested for  
216 two purposes: to determine the relationship between  $E_{obs}$  and  $S_v$  from a comparison  
217 with a pre-flight test, and to determine the maximum pulse width that the signal  
218 processing unit can take in. We vary the input pulse width and the amplitude (Table 2).

219 Second, gaussian-shaped waveforms are tested as a realistic return pulse from the rough  
220 and undulated surface of Ryugu. We similarly vary the full width and the peak amplitude  
221 of gaussian pulses (Table 2). Third and fourth, triangular-shaped waveforms whose  
222 amplitudes increase or decrease with time are tested. For those ascending and descending  
223 pulses, three peak amplitude levels are set with variable full width (Table 2). For all  
224 combinations of amplitude and width, we have measured about 60 pairs of  $D_R$  and  $S_v$ .  
225 Figure 2 shows examples of the four types of the pulse shape recorded in the oscilloscope.

226

### 227 3.2.2 The results of the experiment

228

229 Firstly, we estimate the maximum pulse width that the LIDAR receiver can take in using  
230 the rectangular pulses. Figure 3 shows the relation between the pulse width and  $D_R$  for  
231 the rectangular pulses. This figure indicates that the  $D_R$  becomes saturated when the  
232 pulse width is longer than 90 ns (vertical dashed line in Fig. 3). This limit occurs probably  
233 because the input laser pulse longer than 90 ns is truncated in the signal processing unit  
234 of the LIDAR.

235

236 Figure 4 shows the relations between  $D_R$  and  $S_v$  for the four types of input pulses.

237 Figure 4a shows the relation using 3089 measurements excluding the saturated  $D_R$  and

238 low signal to noise ratio (S/N) data. Figure 4b shows 1639 data whose width is shorter

239 than 90 ns. The widths of gaussian and triangular pulses are measured for the range where

240 the amplitude is higher than the noise floor (Fig. 2). We find a clear relation between  $D_R$

241 and  $S_v$  for the pulses shorter than 90 ns regardless of the pulse shape.

242

243 Next, we need to translate  $S_v$  of Figure 4b into  $E_{obs}$ . However, the relationship of  $D_R$ ,

244  $S_v$ , and  $E_{obs}$  is determined for only 10-ns rectangular pulses in the pre-flight test

245 (Yamada et al., 2017). Therefore, we derive a constant proportionality between  $S_v$  and

246  $E_{obs}$  from 10-ns rectangular pulses, and apply it to all other data shown in Figure 4b.

247 Yamada et al. (2017) show a relationship between  $E_{obs}$  and  $D_R$  of specifically 10-ns

248 rectangular pulses, namely,  $E_{obs}^{rec}$  and  $D_R^{rec}$ , as

249

250 
$$E_{obs}^{rec}(D_R^{rec}) = \frac{R_s(D_R^{rec})\sigma_R}{G} \quad (5)$$

251

252 where  $G$  is the responsivity of the APD and was set as the low-level in the test (Table 1).

253  $\sigma_R$  is the pulse width (10 ns) and  $R_S(D_R^{rec})$  is the conversion function from  $D_R^{rec}$  to the

254 output peak voltage of the APD,

255

$$\begin{aligned} 256 \quad R_S(D_R^{rec}) = & -6.79 \times 10^{-11} D_R^{rec4} + 1.10 \times 10^{-7} D_R^{rec3} - 5.40 \times 10^{-6} D_R^{rec2} + \\ 257 \quad & 1.36 \times 10^{-3} D_R^{rec} + 2.92 \times 10^{-2} \quad (6) \end{aligned}$$

258

259 (Yamada et al., 2017). In the LIDAR-EM experiment, 35 pairs of  $D_R^{rec}$  and  $S_v^{rec}$  are

260 taken for a 10-ns rectangular pulse. By substituting those  $D_R^{rec}$  into Equations (5) and

261 (6), the relation between  $S_v^{rec}$  and  $E_{obs}^{rec}$  is derived (Fig. 5). We estimate the error of

262  $E_{obs}^{rec}$  in Section 3.5.2. Using such error as a weight, the constant proportionality of  $S_v^{rec}$

263 and  $E_{obs}^{rec}$  is derived. Applying this proportionality to all four types of waveforms,

264

$$265 \quad E_{obs} = 1.09 \times 10^{-6} S_v \quad (7).$$

266

267 is obtained. Then Figure 6 is drawn from Figure 4b.  $E_{obs}$  in Figure 6 can be fitted by a

268 fifth polynomial equation (red line) as

269

$$270 \quad E_{obs}(D_R) = 8.38 \times 10^{-25} D_R^5 - 7.45 \times 10^{-22} D_R^4 + 2.23 \times 10^{-19} D_R^3 - 2.34 \times$$

$$271 \quad 10^{-17} D_R^2 + 1.19 \times 10^{-15} D_R - 5.40 \times 10^{-15} \quad (8).$$

272

273 Equation (8) is given for the low responsivity of the APD. For middle and high APD

274 responsivities, the right-hand side of this equation shall be amplified by the ratios of

275 responsivity in Table 1.

276

### 277 **3.3.Calculation of $E_{cal}$ using shape model**

278

279 If the asteroid surface is flat,  $f_{eff}$  in Equation (4) can be simply determined by an

280 incidence angle, reflection law, and the distance between the spacecraft and the asteroid.

281 However, for the very rough surface of Ryugu,  $f_{eff}$  is significantly influenced by the

282 local topography of boulders. For the purpose of studying the composition of surface

283 materials from albedo, we need to eliminate such a topographic effect. Then we include

284 waveform simulation in the following calculation of  $f_{eff}$ .

285

286 3.3.1 Waveform simulation

287

288 As shown in Fig. 4, we exclude return pulse longer than 90 ns from our analysis.

289 However, Hayabusa2 LIDAR does not have a function to measure the waveform of the

290 return pulse, instead, we estimate the temporal profile of return pulse from a waveform

291 simulation. Let us suppose the transmitted laser pulse to have a temporal profile,  $E_T \tau(t)$ .

292 The function  $\tau(t)$  represents the normalized time-wise intensity profile of the

293 transmitted laser beam.  $t$  is the time from the beginning of laser transmission. We adopt

294 the representative transmitted waveform derived from the thermal vacuum test and

295 normalize it so that the total energy of the entire waveform is unity (Fig. 7).

296

297 The laser beam emitted from the LIDAR transmitter is reflected and scattered at the

298 undulating surface of Ryugu. Only a tiny fraction of the laser emission finally incidents

299 into the receiving telescope. The laser footprint is a circle on the surface of Ryugu, which  
300 corresponds to a part of the field of view (FOV) of the receiving telescope because FOV  
301 is narrower than the full beam divergence of the transmitter (Table 1). The surface  
302 undulations within the footprint disturb the waveform of the return pulse. To simulate  
303 Ryugu topography, we use a shape model developed from the images taken by the ONC  
304 (Watanabe et al., 2019). The laser footprint is divided into small area elements. For each  
305 element, the return pulse waveform is calculated considering the projected beam pattern  
306 (Fig. 8), distance and direction from LIDAR, and the reflection property of each element.  
307 Finally, the return pulse waveform is calculated by summing them up in the footprint area.

308

309  $f_{eff}$  in Equation (4) is expressed as a time integration of normalized return pulse  
310 waveform.

311

$$312 \quad f_{eff} = \sum_{t=t_s}^{t=t_e} \sum_{xy} \xi_{xy} \eta_{xy} \varepsilon_{xy} \Delta_{xy} \tau(t - 2L_{xy}/c) \Delta t \quad (9)$$

313

314 where,  $t_s$  and  $t_e$  are the start and end times of the received return pulse, respectively,

315  $\Delta t$  is a time interval of numerical integration, and  $c$  is the speed of light.  $\Delta_{xy}$  is an area  
316 of the small element within the laser footprint on the Ryugu surface and  $L_{xy}$  is the  
317 distance between the LIDAR telescope and  $\Delta_{xy}$ .  $\varepsilon_{xy}$  is the normalized beam pattern of  
318 the transmitted laser pulse in  $\Delta_{xy}$  (Fig. 8).  $\xi_{xy}$  is a factor that depends on the law of  
319 reflection. We apply two types of reflection law, i.e., Lambert and Lommel-Seeliger, and  
320 compare the results (see Section 5).

321

$$322 \quad \xi_{xy} = \frac{\cos\theta_{xy}}{\pi} \text{ (Lambert law)}$$

$$323 \quad \xi_{xy} = \frac{1}{\pi} \text{ (Lommel-Seeliger law)} \quad (10)$$

324

325 where,  $\theta_{xy}$  is the incident angle of the laser on  $\Delta_{xy}$ .  $\eta_{xy}$  is the solid angle of the  
326 LIDAR telescope viewed from  $\Delta_{xy}$ , and it is expressed as follows,

327

$$328 \quad \eta_{xy} = \frac{A_0}{L_{xy}^2} \quad (11)$$

329

330 where  $A_0$  is the aperture area of the receiving FAR telescope, and is 0.0095 m<sup>2</sup> as listed

331 in Table 1.

332

333 The  $\theta_{xy}$  and  $L_{xy}$  in Equations (10) and (11) are dependent on the topographic  
334 undulations of Ryugu. These values are obtained from a shape model of Ryugu developed  
335 from ONC images (SHAPE\_SPC\_3M\_v20200323, an updated version of Watanabe et al.,  
336 2019), which consists of 3,145,728 facets and 1,579,014 vertices. As will be stated later,  
337 the area of  $\Delta_{xy}$  on the Ryugu surface is sufficiently smaller than the average area of one  
338 facet of the shape model. Therefore, we regard that  $\Delta_{xy}$  does not span multiple facets in  
339 the shape model. Then  $\theta_{xy}$  and  $L_{xy}$  are calculated from the center of the  $\Delta_{xy}$  to the  
340 spacecraft position estimated by Matsumoto et al. (2020).

341

342 The  $\varepsilon_{xy}$  in Equation (9) is not spatially uniform and varies for each laser transmission.  
343 We averaged 1200 different beam patterns obtained in the thermal vacuum test, and  
344 normalized so that the total energy in the cross-section is unity (Fig. 8). The uncertainty  
345 of the  $\varepsilon_{xy}$  will be discussed in Section 3.5.2. As described above, only part of the beam  
346 is inside of the FOV of the receiving telescope (Fig. 8) and is used for the return pulse

347 calculation.

348

349 We divide the FOV of a diameter of 1.44 mrad into small elements of an area of (5.58  
350  $\times 10^{-3})^2$  mrad<sup>2</sup> (the right of Fig. 8). Each element corresponds to a footprint element  $\Delta_{xy}$   
351 at the surface of Ryugu. The area of  $\Delta_{xy}$  is in the range between 0.0025 to 0.0031 m<sup>2</sup>  
352 depending on the altitude between 1 and 9 km. Thus  $\Delta_{xy}$  is small enough compared with  
353 the average area of facets of the shape model of 0.89 m<sup>2</sup>.

354

355 Due to the surface topography of Ryugu, the value of  $L_{xy}$  differs for each  $\Delta_{xy}$ . As a  
356 result, the laser reflection time at the surface and the reception time at the LIDAR  
357 telescope also differ for each  $\Delta_{xy}$ . This delay of time appears in Equation (9) as  $\tau(t -$   
358  $2L_{xy}/c)$ .  $\Delta t$  in Equation (9) is set as  $2.5 \times 10^{-11}$  s which corresponds to 0.0075 m in the  
359 distance for the speed of light and is small enough to evaluate 90-ns criteria of the return  
360 pulse.

361

362 Figure 9 shows examples of the calculated waveform of return pulses and the

363 topography of the Ryugu shape model within the laser footprints. The topography in the  
364 right example is more undulated than that in the left one. Thus, in the right example, the  
365 waveform deviates from the transmitted pulse shown in Figure 7, while the left examples  
366 are similar to the gaussian form. Note that the amplitude of the return pulse is smaller in  
367 the right example than in the left one because the observation altitude is different.

368

369 3.3.2. Re-evaluation of  $E_T$  from  $D_T$

370

371 The conversion function from  $D_T$  to  $E_T$  has been determined by a thermal vacuum  
372 test conducted before the Hayabusa2 launch. Figure 10 shows the measurements of  $E_T$   
373 and  $D_T$ . The straight blue line is derived by fitting a linear equation in our previous study  
374 (Yamada et al., 2017). In this study, we adopt the 3rd polynomial equation to fit better the  
375 experiment results (the black solid curve in Fig. 10).

376

$$377 \quad E_T(D_T) = -6.04 \times 10^{-7} D_T^3 + 2.36 \times 10^{-4} D_T^2 - 3.05 \times 10^{-2} D_T + 1.32$$

378

(12).

379

380 This equation does not depend on temperature; however, we find that in-situ observational  
381 data are influenced by heater cycles of LIDAR. We will discuss this point later in Section  
382 3.4.

383

384 In the thermal vacuum test, we have measured  $D_T$  ranging from 115 to 136. In  
385 principle,  $E_T$  increases with  $D_T$ . However, for the  $D_T$  smaller than 117, the experiment  
386 results show that  $E_T$  decreases as  $D_T$  increases (Fig. 10). Such behavior is  
387 unreasonable; thus, we exclude the results of  $D_T$  below 117 in the derivation of Equation  
388 (12). Accordingly, we exclude data sets whose  $D_T$  is lower than 117, as described in  
389 chapter 4.

390

### 391 **3.4 The calculation and correction of albedo**

392

393 The upper panel of Figure 11a represents a time series albedo calculated from the data  
394 acquired on 20 July 2018 as an example. There is an obvious periodic variation in the

395 albedo with frequency of around 400 s. A periodic variation with the same frequency is  
396 also seen in the time series transmitted energy (Figure 11b upper panel).

397 These periodic variations are synchronized with the heater cycle. Figure 11b bottom  
398 panel shows the time series temperature of laser diode (LD) for the transmitter. Thus the  
399 periodic variation is artificial, therefore we eliminate these frequency components.

400 Because the heater cycle depends on the thermal condition of the LIDAR, the frequency  
401 components from 0.02 Hz to 0.0032 Hz are removed from the calculated albedo using  
402 low-pass and high-pass filters. The bottom panel of Figure 11a shows the corrected albedo  
403 after removing the periodic components.

404

### 405 **3.5 Error of albedo derivation**

406

407 From Equation (3), an error of normal albedo,  $\delta\rho$ , can be evaluated by the following  
408 equation;

409

$$410 \quad \frac{\delta\rho}{\rho} = \sqrt{\left(\frac{\delta E_{obs}}{E_{obs}}\right)^2 + \left(\frac{\delta E_{cal}}{E_{cal}}\right)^2} \quad (13)$$

411

412 where  $\delta E_{obs}$  and  $\delta E_{cal}$  are errors of  $E_{obs}$  and  $E_{cal}$ , respectively.

413

414 3.5.1 Error of  $E_{obs}$

415

416  $\delta E_{obs}$  is derived from Figure 6, while an error of each point in Figure 6 is evaluated

417 from Figure 5. On the other hand, errors of the points in Figure 5,  $\delta E_{obs}^{rec}$ , is derived from

418 Equation (5).

419

$$420 \quad \frac{\delta E_{obs}^{rec}}{E_{obs}^{rec}} = \sqrt{\left(\frac{\delta G}{G}\right)^2 + \left(\frac{\delta R_S(D_{obs}^{rec})}{R_S(D_{obs}^{rec})}\right)^2} \quad (14)$$

421

422 where  $\delta G$  is the error of responsivity of the APD in low gain and is 9.0 % (Table 1).

423  $\delta R_S(D_{obs}^{rec})$  is the fitting error of  $R_S(D_{obs}^{rec})$  in Equation (6) in low gain, and is 3.7 %

424 (Yamada et al., 2017). Then,  $\delta E_{obs}^{rec}/E_{obs}^{rec}$  is 9.7 %.

425

426 All points in Figure 5 are attached with 9.7 % error bars. Then, the ratio of  $E_{obs}$  and

427  $S_v$  is calculated with this weight. Consequently, the standard deviation of this fitting is  
 428 evaluated as much as 19.2 %. Using this 19.2 % error as weight, Equation (8) is derived.  
 429 Then,  $\delta E_{obs}/E_{obs}$  becomes 15.3 %.

430

### 431 3.5.2 Error of $E_{cal}$

432

433 Following Equation(4),  $\delta E_{cal}$  is expressed as

434

$$435 \quad \frac{\delta E_{cal}}{E_{cal}} = \sqrt{\left(\frac{\delta E_T}{E_T}\right)^2 + \left(\frac{\delta f_{eff}}{f_{eff}}\right)^2} \quad (15)$$

436

437 where  $\delta E_T$  is the random error of  $E_T$ ,  $\delta f_{eff}$  is the error of  $f_{eff}$ .  $\beta$  has been  
 438 precisely measured as shown in Table 1, therefore is not included in Equation (15).  $\delta E_T$   
 439 is calculated as fitting error of Equation (12) (Fig. 3). Using 1802 data sets included in  
 440 Figure 10,  $\delta E_T/E_T$  of 1.78 % is derived.

441

442  $f_{eff}$  in Equation (9) includes six variables:  $\xi_{xy}$ ,  $\eta_{xy}$ ,  $\tau(t)$ ,  $L_{xy}$ ,  $\varepsilon_{xy}$  and  $\Delta_{xy}$ . In the

443 case of the Lommel-Seeliger law, which we prefer to the Lambert model as described  
444 later,  $\xi_{xy}$  is a constant (Equation (10)). Then,  $\eta_{xy}$ , and  $\Delta_{xy}$  are functions of  $L_{xy}$   
445 (Section 3.3.1). Thus,  $\delta f_{eff}$  is dependent on  $\varepsilon_{xy}$ ,  $\tau(t)$  and  $L_{xy}$ . Since it is difficult to  
446 calculate these three errors directly, we calculate  $E_{cal}$  values by changing  $\varepsilon_{xy}$ ,  $\tau(t)$   
447 and  $L_{xy}$ , respectively, within possible ranges.

448

449 To investigate an error due to dispersion of  $\varepsilon_{xy}$ , we have calculated  $E_{cal}$  using 1200  
450 different beam patterns for one specific location and have obtained the deviation of 2.4 %.  
451 We have repeated the same evaluations for several other locations measured in different  
452 terrains and have obtained similar results.

453

454 Similarly, for  $\tau(t)$ , we have calculated  $E_{cal}$  using intensity profiles of 1200 different  
455 measurements in the thermal vacuum test for several locations. Then, deviation of  $E_{cal}$   
456 is evaluated to be less than 0.5 %.

457

458 For the error of  $L_{xy}$ , both uncertainties of the spacecraft orbit and the shape model need

459 to be considered. According to Yamamoto et al. (2020), the errors of the spacecraft orbit  
460 (Matsumoto et al. (2020)) are 1.95 m in the direction of the transmitted laser. Watanabe  
461 et al. (2019) compare the heights of some boulders in the shape model constructed by the  
462 SPC (stereo photo clinometry) method with the laser ranging data of LIDAR. It has shown  
463 that the shape model has an uncertainty of about 2 m. Then, we take 2.79 m as the error  
464 of  $L_{xy}$  from a root of the mean square of the orbital and shape model errors. Similar to  
465  $\varepsilon_{xy}$  and  $\tau(t)$ ,  $E_{cal}$  are also calculated by changing  $L_{xy}$  within range of  $\pm 2.79$  m at  
466 both the lowest and highest altitudes, those are, 1066 m and 9000 m. Then, the variations  
467 of  $E_{cal}$  are 0.52 % for the lowest altitude and 0.062 % for the highest altitude.

468

469 In the above argument, we consider the  $L_{xy}$  error only in the line-of-sight. However,  
470 the spacecraft orbit and the shape model have errors in a horizontal direction, too. These  
471 errors result in uncertainty of the location of a laser footprint. Besides, the real Ryugu  
472 topography within the footprint may be different from the shape model. Though the error  
473 of  $L_{xy}$  in the horizontal direction is not calculated, the uncertainty of the footprint in the  
474 horizontal direction is discussed in Section 6. In total,  $\delta f_{eff}/f_{eff}$  is derived as 2.51 %

475 from the RMS errors of  $\varepsilon_{xy}$ ,  $\tau(t)$  and  $L_{xy}$ . Consequently,  $\delta E_{cal}/E_{cal}$  is evaluated as  
476 3.1 %. Finally,  $\delta\rho/\rho$  of 15.6 % is derived from Equation (13) using  $\delta E_{cal}/E_{cal}$  of  
477 3.1 % and  $\delta E_{obs}/E_{obs}$  of 15.3 %.

478

#### 479 **4 Data selection**

480

481 The LIDAR observation of Ryugu started on 26 June 2018 and finished on 14  
482 November 2019.  $D_T$  and  $D_R$  were continuously obtained at a sampling rate of 1/32 Hz  
483 at the home position of the spacecraft, namely at an altitude of about 20 km around the  
484 equator of Ryugu (Watanabe et al., 2019). However,  $D_R$  obtained at the home position  
485 are between 5 and 20 DU, too low to estimate albedo considering measurement errors  
486 described in Section 3.5. In contrast, in some special operations such as touchdown and  
487 gravity measurement, the spacecraft descended from the home position to altitude below  
488 10 km, acquiring  $D_T$  and  $D_R$  at a rate of 1 Hz. We use only such data taken at altitudes  
489 lower than 9 km by FAR telescope. Using this criterion,  $D_R$  are constrained between 100  
490 and 200 DU, and sufficiently high S/N is secured.

491

492 Besides, we limit the data to those obtained before a conjunction that continued from  
493 the end of November to the end of December in 2018 because the FAR telescope of the  
494 LIDAR is likely contaminated by surface regolith flown by the first touchdown in  
495 February 2019. Before the conjunction, low and middle-altitude operations were carried  
496 out on 15 days (Table 3). These observations cover only the areas around the equator  
497 where the special operations were carried out.

498

499 As described in Section 3.2,  $D_R$  whose widths are longer than 90 ns are eliminated  
500 from our analysis. In addition, we remove  $D_R$  more than 250 to avoid saturation and  $D_T$   
501 less than 117 as described in Section 3.3.2. Finally, we have obtained the 390,456 sets of  
502  $D_T$  and  $D_R$ , that is about 44 % of total observation data.

503

## 504 **5 Results**

505

### 506 **5.1 Reflectance model of Ryugu**

507

508 First, we compare and evaluate Lambert and Lommel-Seeliger reflection laws. These  
509 laws have different dependencies on the incident angle (Eq. (10)). Then, we plot albedos  
510 calculated based on these two laws with respect to the incident angle, as shown in Figure  
511 12. For the Lambert law, the albedo values systematically increase with incident angle.  
512 On the other hand, for the Lommel-Seeliger law, the values are randomly distributed  
513 around an average without dependence of incident angle. Therefore, we conclude that the  
514 Lommel-Seeliger law is preferable to the Lambert law for Ryugu. Furthermore, the  
515 photometric characteristic of Ryugu obtained by ground-based observations also supports  
516 the Lommel-Seeliger model (Le Corre et al., 2018). Thus, we adopt the Lommel-Seeliger  
517 law in the following calculation of the albedo.

518

## 519 **5.2 The albedo map around the equator**

520

521 Figure 13 shows all calculated albedo values for each footprint after the correction of  
522 periodic variation. Because neighboring footprints are overlapped depending on their

523 sizes, we average albedo within a square grid of  $2^\circ$  by  $2^\circ$ . For example, the diameter of  
524 the laser footprint at an altitude of 9 km is about 11.2 m. On the other hand, the length of  
525  $1^\circ$  in latitude on Ryugu is about 7.5 m assuming a sphere. Therefore, each  $2^\circ$  by  $2^\circ$  grid  
526 can include the diameter of laser footprint at an altitude lower than 9 km. Next, we count  
527 the number of footprints whose centers are located in the grid for each  $2^\circ$  by  $2^\circ$  grid and  
528 map those numbers in Figure 14. The largest number is 627. This grid is located around  
529 the equator where observations were most frequently made. Next, we eliminate the grids  
530 whose footprints are less than 3. Then, the number of the averaged grids is 3946.

531

532 The averaged grids are distributed between  $40^\circ\text{S}$  and  $20^\circ\text{N}$  on Ryugu, shown in Figure  
533 15a. The average and standard deviation are 0.0406 and 0.0031 (7.6 % deviation) among  
534 all grids. Figure 15b also shows standard deviations of albedo. Some grids include large  
535 boulders resulting in large deviations, probably because their reflection is not reproduced  
536 well in the waveform simulation. This point is further discussed in the following chapter.

537

538 Figure 16 shows a histogram of the albedo. Note that the vertical axis is on a log scale.

539 About 98 % of the averaged grids have values between 0.03 and 0.05. The mode is 0.0425.

540 The largest bin is between 0.040 and 0.045, including 52 % of all counts.

541

## 542 **6 Discussion**

543

544 The albedo maps of Ryugu are also produced from Hayabusa2 ONC-T images (Yokota

545 et al., 2021). The ONC-T has seven broadband filters ranging in wavelength from 0.3975

546  $\mu\text{m}$  to 0.9451  $\mu\text{m}$  (Tatsumi et al., 2020). The latter is the closest to the wavelength to

547 LIDAR. The global average of the normal albedo obtained by the ONC-T at 0.9451  $\mu\text{m}$

548 is  $0.0399 \pm 0.0005$  (Yokota et al., 2021), which overlaps with our result of  $0.0406 \pm$

549  $0.0031$  within  $1\sigma$ . Both Sugita et al. (2019) and Tatsumi et al. (2020) indicate flat spectral

550 features in the visible range of ONC-T, and it appears that, at least, this flatness continues

551 till near-infrared wavelength around the equator.

552

553 Figures 15a and 16 show low and uniform albedo, consistent with observations of ONC

554 and NIRS3 of Hayabusa2 (Sugita et al., 2019, Kitazato et al., 2019). Also, such albedo

555 uniformity is comparable to that of C-type asteroid 253 Mathilde observed at 0.55  $\mu\text{m}$  by  
556 NEAR Shoemaker (Clark et al., 1999), although albedo maps derived from the  
557 Hayabusa2 mission have higher resolution. In the OSIRIS-REx mission, another albedo  
558 map of the C-type asteroid Bennu has been constructed using onboard camera images  
559 (Golish et al., 2021). Bennu's albedo distribution histogram has a median value of  
560  $0.046 \pm 0.002$  in the visible range. And it is also similar to that of Ryugu. All remote  
561 sensing data, including our results, indicate such low albedo of C-type asteroids.

562

563 There are exceptional grids that show albedo deviated from the global average of over  
564 3s. Four high albedo grids and 33 low albedo grids are listed in Table 4. The highest  
565 albedo is 0.0720 at 35°S and 99°E (grid number 1 in Table 4). Such high albedo may be  
566 influenced by Ejima Saxum, an extraordinary large (70 m in diameter) Type 1 boulder  
567 (Sugita et al., 2019). This type of boulder is dark and possesses rugged surfaces and edges.  
568 The standard deviation in this grid (0.0542) is also the largest of all grids. The 0.9451  $\mu\text{m}$   
569 albedo in Ejima Saxum region does not indicate such high values, but it is slightly darker  
570 than the average (Yokota et al., 2021). Waveform simulation of returned pulses from this

571 grid indicates that multiple reflections due to complex topography possibly result in a  
572 large albedo deviation.

573

574 The lowest albedo is  $0.0199 \pm 0.0072$  (grid number 27 in Table 4) and is observed  
575 around  $7^{\circ}\text{N}$  and  $155^{\circ}\text{E}$ . This grid is located within Kintaro crater, 170 m in diameter. This  
576 area is also darker than the surroundings in the  $0.5489\ \mu\text{m}$  albedo map (Yokota et al.,  
577 2021). However, other low albedo grids in Table 4 are not necessarily dark in the ONC-  
578 T albedo map (Yokota et al., 2021).

579

580 There are two possible causes of these high and low albedos. One is some high incident  
581 angles, as listed in Table 4. If the laser shots hit the side of small boulders or steep slopes,  
582 which the shape model cannot represent, it becomes difficult to trace rays. Another is the  
583 uncertainty of laser footprint locations in a horizontal direction as described in Section  
584 3.5.2. The spacecraft position has an error of  $0.143^{\circ}$  in a direction perpendicular to  
585 transmitted laser in an asteroid-centered coordinate system (Yamamoto et al., 2020). The  
586 shape model of Ryugu also has an error in the horizontal direction (Noda et al., 2021). If

587 there is a misalignment between the true location of a laser footprint and the estimation,  
588 it may result in albedo errors, especially in complicated surface terrain areas.

589

590 If the high and low albedos are real, they indicate an unusual property of the surface  
591 materials. The dark spots detected by LIDAR but not by ONC may indicate weak  
592 reflectance at 1.064  $\mu\text{m}$  compared with that at visible wavelength. Nevsvorny et al. (2005)  
593 describe the reflectance of C-complex decrease at near-infrared wavelength due to space  
594 weathering. Or the reflectance at 1.064  $\mu\text{m}$  could be an indicator of olivine and pyroxene.  
595 Detailed comparison and combination with the ONC image and other reflectance data  
596 will be important to reveal the causes of the exceptional albedo spots.

597

598 Though the uncertainty is large, we also see small albedo variations between 0.03 and  
599 0.05. Because there remain unanalyzed intensity data of Hayabusa2 LIDAR, which cover  
600 a broader area after the conjunction, further investigation of global albedo variation may  
601 help us understand surface processes on Ryugu.

602

## 603 7 Conclusion

604

605 We have successfully observed laser intensities returned from the C-type asteroid Ryugu  
606 by the Hayabusa2 LIDAR. We have established the method to derive albedo using the  
607 observed intensities and the return pulse simulation. This is the first attempt to derive the  
608 albedo at 1.064  $\mu\text{m}$  on Ryugu. Our analysis covers areas around the equator between  
609 about 40°S and 20°N. Each albedo is evaluated in the grid of 2° by 2°. Using 3946 grids  
610 with more than three footprints, the global average and the error of albedo is determined  
611 as  $0.0406 \pm 0.0031$ . About half of the selected grids have albedo values in the range of  
612 0.04-0.045. This low and uniform albedo is consistent with the observation by ONC and  
613 NIRS3. This similarity suggests that our derivation method is useful to evaluate the  
614 albedo of the very rough surface by the laser altimeter. For example, this new  
615 methodology can be applied if the future middle and small class missions adopt the  
616 LIDAR as simple as the one onboard Hayabusa2. Our albedo map shows some  
617 exceptional spots. Further investigations using more LIDAR and ONC data will improve  
618 our understanding of the albedo variation on the C-type asteroid.

619

620

621

622 **Declarations**

623 **Ethics approval and consent to participate**

624 Not applicable

625 **Consent for publication**

626 Not applicable

627 **List of abbreviations**

628 APD: avalanche photodiode

629 DU: digital unit

630 EM: engineering model

631 FOV: field of view

632 GSE: ground support equipment

633 LD: laser diode

634 LIDAR: light detection and ranging

635 LOLA: Lunar orbiter laser altimeter

636 MLA: Mercury laser altimeter

637 NIRS3: near infrared spectrometer

638 OLA: OSIRIS-REx laser altimeter

639 ONC: optical navigation camera

640 ONC-T: optical navigation camera for telescopic nadir view

641 RMS: root mean square

642 SPC: stereo photo clinometry

643 S/N: signal to noise ratio

644 TIR: thermal infrared imager

645

646 **Availability of data and materials**

647 The dataset of the Hayabusa2 LIDAR and related SPICE

648 kernels used in this study are currently under review to be

649 opened in Planetary Data System.

650

651

652 **Competing interests**

653 This article does not relate with any competing interests.

654

655 **Funding**

656 The operation of Hayabusa2 including the LIDAR observation had been  
657 performed by financial support of JAXA Hayabusa2 project.

658

659 **Authors' contributions**

660 RY led the coauthors in data acquisition, analysis, and manuscript writing  
661 in this original paper. KY coded waveform simulation and wrote related  
662 sections 3.3 and 3.5.1. HA analyzed the parts of data in the LIDAR-EM  
663 experiment and supported the writing of sections 3.2 and 3.5.2. SO studied  
664 the albedo map and exceptional albedo spots and was a major contributor  
665 in writing Chapters 5 and 6. HS and HN supported the LIDAR-EM  
666 experiments and operations of the LIDAR during rendezvous with Ryugu.

667 KM provided orbital information of the spacecraft, and NH disclosed  
668 details of the Ryugu shape model. Asteroid science and characteristic of the  
669 C-type asteroid were written in cooperation with FY and SS. SA provided  
670 helpful information about the LIDAR of the former Hayabusa project. NN  
671 and TM are science and engineering PIs of the Hayabusa2 LIDAR.

672

### 673 **Acknowledgements**

674 We appreciate financial and technical support from the Hayabusa2 project of  
675 the Japan Aerospace Exploration Agency (JAXA). Furthermore, we are  
676 grateful to Dr. Yasuhiro Yokota in JAXA for constructive discussion and for  
677 providing the results related to the ONC-T normal albedo.

678

### 679 **Authors' information**

680 1. The University of Aizu, Tsuruga, Ikki-machi, Aizu-Wakamatsu,

681 Fukushima 965-8580, Japan.

682 2. National Astronomical Observatory of Japan, 2-21-1 Osawa, Mitaka,

- 683 Tokyo 181-8588, Japan.
- 684 3. Institute of Space and Astronautical Science, Japan Aerospace  
685 Exploration Agency, 3-1-1 Yoshinodai, Chuo-ku, Sagamihara, Kanagawa  
686 252-5210, Japan.
- 687 4. National Astronomical Observatory of Japan, 2-21-1 Osawa, Mitaka,  
688 Tokyo 181-8588, Japan.
- 689 The Graduate University for Advanced Studies, SOKENDAI, Hayama,  
690 Kanagawa 240-0193, Japan.
- 691 5. Chiba Institute of Technology, 2-17-1 Tsudanuma, Narashino, Chiba  
692 257-0016, Japan.
- 693 6. National Astronomical Observatory of Japan, 2-12 Hoshigaoka,  
694 Mizusawa-ku, Oshu, Iwate 023-0861, Japan.
- 695 The Graduate University for Advanced Studies, SOKENDAI, Hayama,  
696 Kanagawa 240-0193, Japan.
- 697 7. National Astronomical Observatory of Japan, 2-21-1 Osawa, Mitaka,  
698 Tokyo 181-8588, Japan.

699 The Graduate University for Advanced Studies, SOKENDAI, Hayama,  
700 Kanagawa 240-0193, Japan.

701 8. National Astronomical Observatory of Japan, 2-12 Hoshigaoka,  
702 Mizusawa-ku, Oshu, Iwate 023-0861, Japan.

703 The Graduate University for Advanced Studies, SOKENDAI, Hayama,  
704 Kanagawa 240-0193, Japan.

705 9. University of Occupational and Environmental Health, 1-1 Iseigaoka,  
706 Yahatanisi-ku, Kitakyushu, Fukuoka 807-8555, Japan.

707 Chiba Institute of Technology, 2-17-1 Tsudanuma, Narashino, Chiba 257-  
708 0016, Japan.

709 10. Nihon University, 7-24-1 Narashinodai, Funabashi, Chiba 274-8501,  
710 Japan

711 11. The University of Aizu, Tsuruga, Ikki-machi, Aizu-Wakamatsu,  
712 Fukushima 965-8580, Japan.

713 12. Osaka University, 1-1 Machikaneyama, Toyonaka, Osaka 560-0043,  
714 Japan.

715 13. Institute of Space and Astronautical Science, Japan Aerospace  
716 Exploration Agency, 3-1-1 Yoshinodai, Chuo-ku, Sagamihara, Kanagawa  
717 252-5210, Japan.

718

719

720 **References**

721 S. Abe, T. Mukai, N. Hirata et al. (2006) Mass and local topography measurements of  
722 Itokawa by Hayabusa. *Science* 312, pp.1344-1347

723

724 O.S. Barnouin, M. G. Daly, E. E. Palmer et al. (2020) Digital terrain mapping by the  
725 OSIRIS-REx mission. *Planetary and Space Science* 180, 104764, pp.1-16

726

727 R. P. Binzel, A. Morbidelli, S. Merouane, F. E. Demeo, M. Birlan, P. Vernazza, C. A.  
728 Thomas, A. S. Rivkin, S. J. Bus, A. T. Tokunaga (2010) Earth encounters as the origin of  
729 fresh surfaces on near-Earth asteroid. *Nature* 463, pp.331-334

730

731 S. J. Bus, R. P. Binzel (2002) Phase II of the small main-belt asteroid spectroscopic survey:  
732 a feature-based taxonomy. *Icarus* 158, 1, pp.146-177  
733  
734 B.E. Clark, J. Veverka, P. Helfenstein, P. C. Thomas, J. F. Bell III., A. Harch, M. S.  
735 Robinson, S. L. Murchie, L. A. McFadden, C. R. Chapman (1999) Near photometry of  
736 asteroid 253 Mathilde. *Icarus* 140, pp.53-65  
737  
738 M.G. Daly, O.S. Barnouin, C. Dickinson et al. (2017) The OSIRIS-REx laser altimeter  
739 (OLA) investigation and instruments, *Space and Science Review*, 212, pp.899-924  
740  
741 D.R. Golish, N.K. Shultz, T.L. Becker et al. (2021) A high-resolution normal albedo map  
742 of asteroid (101955) Bennu, 355, 114133, p.1-18  
743  
744 K. Kitazato, B. E. Clark, M. Abe, S. Abe, Y. Takagi, T. Hiroi, O. S. Barnouin-Jha, P. A.  
745 Abell, S. M. Lederer, F. Vilas (2008) Near-infrared spectrophotometry of asteroid 25143  
746 Itokawa from NIRS on the Hayabusa spacecraft. *Icarus* 194, pp.137-145

747

748 K. Kitazato, R. E. Milliken, T. Iwata et al. (2019) the surface composition of asteroid  
749 162173 Ryugu from Hayabusa2 near-infrared spectroscopy. *Science* 364, pp.272-275

750

751 L. Le Corre, J. A. Sanchez, V. Reddy, D. Takir, E. A. Cloutis, A. Thirouin, K. J. Becker,  
752 J. Li, S. Sugita, E. Tatsumi (2018) Ground-based characterization of Hayabusa2 mission  
753 target asteroid 162173 Ryugu: constraining mineralogical composition in preparation for  
754 spacecraft operations. *Monthly Notices of the Royal Astronomical Society* 475, 1,  
755 pp.614-623

756

757 K. Matsumoto, H. Noda, Y. Ishihara et al. (2020) Improving Haysabu2 trajectory by  
758 combining LIDAR data and a shape model, *Icarus* 338(1), 113574

759

760 T. Mizuno, T. Kase, T. Shiina, M. Mita, N. Namiki, H. Senshu, R. Yamada, H. Noda, H.  
761 Kunimori, N. Hirata, F. Terui, Y. Mimasu (2017) Development of the laser altimeter  
762 (LIDAR) for Hayabusa2. *Space Sci. Rev.* 208, pp.33-34

763

764 T. Mukai, S. Abe, N. Hirata et al. (2007) An overview of the LIDAR observations of  
765 asteroid 25143 Itokawa. *Adv. Space Res.* 40, pp.187-192

766

767 D. Nesvorny, R. Jedicke, R. J. Whiteley, Z. Ivezić (2005) Evidence for asteroid space  
768 weathering from the Sloan Digital Sky Survey. *Icarus* 173, pp.132-152

769

770 G. A. Neumann, J. F. Cavanaugh, X. Sun, E. Mazarico, D. E. Smith, M. T. Zuber, D. Mao,  
771 D. A. Paige, S. C. Solomon, C. M. Ernst, O. S. Barnouin (2013) Bright and dark polar  
772 deposits on Mercury: evidence for surface volatiles. *Science* 339, pp. 296-300

773

774 G. A. Neumann, M. K. Barker, E. Mazarico, M. G. Daly, O. S. Barnouin, E. R. Jawin, D.  
775 S. Lauretta (2020) Global and local variations in 1064 nm normal albedo of Bennu from  
776 the OSIRIS-REx laser altimeter. Abstract of 51st Lunar and Planetary Science Conference,  
777 2032.

778

779 H. Noda, H. Senshu, K. Matsumoto et al. (2021) Alignment determination of the  
780 Hayabusa2 laser altimeter (LIDAR). *Earth Planets Space* 73, 21,  
781 <https://doi.org/10.1186/s40623-020-01342-8>

782

783 V. Reddy, A. Nathues, L. Corre et al. (2012) Color and albedo heterogeneity of Vesta from  
784 Dawn. *Science* 336, pp.700-703

785

786 H. Senshu, S. Oshigami, M. Kobayashi, R. Yamada, N. Namiki, H. Noda, Y. Ishihara, T.  
787 Mizuno (2017) Dust detection mode of the Hayabusa2 LIDAR. *Space Sci. Rev.* 208, pp.65-

788 79

789

790 D. E. Smith, M. T. Zuber, G. B. Jackson et al. (2010) The lunar orbiter laser altimeter  
791 investigation on the lunar reconnaissance orbiter mission. *Space. Sci. Rev.* 150, pp.209-

792 241

793

794 S. Sugita, D. Kuroda, S. Kameda, S. Hasegawa, S. Kamata, M. Abe, M. Ishiguro, N.

795 Takao, M. Yoshikawa (2013) Visible spectroscopic observation of asteroid 162173  
796 (1999ju3) with the Gemini-s telescope, in 44<sup>th</sup> DPS Meeting. American Astronomical  
797 Society (Abstract 102.02).

798

799 S. Sugita, R. Honda, T. Morota et al. (2019) The geomorphology, color, and thermal  
800 properties of Ryugu: implications for parent-body processes. *Science* 364, eaaw0422,  
801 pp.1-11

802

803 X. Sun et al. (2015) Calibration of the Mercury Laser Altimeter on the MESSENGER  
804 spacecraft. *IEEE Trans. Geosci. Remote Sens.* 53(5), pp.2860-2874

805

806 E. Tatsumi, D. Domingue, S. Schröder et al. (2020) Global photometric properties of  
807 (162173) Ryugu. *Astronomy & Astrophysic* 639, A83 pp.1-19

808

809 E. Tatsumi, C. Sugimoto, L. Rui et al. (2021) Collisional history of Ryugu's parent body  
810 from bright surface boulders. *Nature Astronomy* 5, pp.39-45

811

812 F. Vilas (2008) Spectral characteristics of Hayabusa2 near-Earth asteroid targets 162171  
813 1999JU3 and 2001 QC34. *Astron. J.* 135, pp.1101-1105

814

815 S. Watanabe, M. Hirabayashi, N. Hirata et al. (2019) Hayabusa2 arrives at the  
816 carbonaceous asteroid 162173 Ryugu – a spinning top-shaped rubble pile. *Science* 364,  
817 6437, pp.268-272

818

819 R. Yamada, H. Senshu, N. Namiki, T. Mizuno, S. Abe, F. Yoshida, H. Noda, N. Hirata, S.  
820 Oshigami, H. Araki, Y. Ishihara, K. Matsumoto (2017) Albedo observation by Hayabusa2  
821 LIDAR: instrument performance and error evaluation. *Space Sci. Rev.* 208, pp.49-64

822

823 K. Yamamoto, T. Otsubo, K. Matsumoto et al. (2020) Dynamic precise orbit  
824 determination of Hayabusa2 using laser altimeter (LIDAR) and image tracking data sets.  
825 *Earth, Planets and Space*, <https://doi.org/10.1186/s40623-020-01213-2>

826

827 Y. Yokota, R. Honda, E. Tatsumi et al. (2021) Opposition observation of 162173 Ryugu:  
828 normal albedo map highlights variations in regolith characteristics. *The Planetary Science*  
829 *Journal*, 2:177, pp. 1-32

830

831 M. T. Zuber, J. W. Head, D. E. Smith, G. A. Neumann, E. Mazarico, M. H. Torrence, O.  
832 Aharonson, A. R. Tye, C. Fassert, M. A. Rosenburg, H. J. Melosh (2012) Constraints on  
833 the volatile distribution within Shackleton crater at the lunar south pole. *Nature* 486,  
834 pp.378-382

835

836

837 **Preparing illustrations and figures**

838 Figure 1. Schematic diagram of the experimental setup of the LIDAR-EM.

839

840 Figure 2. The examples of four types of input laser pulses in the LIDAR-EM experiment.

841 Solid, dashed, dotted, and dash-dotted lines indicate rectangular, gaussian, ascending

842 triangular, and descending triangular pulses, respectively. Widths and peak amplitudes

843 are 60 ns and 120, 40 ns and 120, 70 ns and 150, and 70 ns and 150, respectively. The

844 horizontal thick dashed line indicates the noise floor of the records.

845

846 Figure 3. The pulse width and  $D_R$  for the rectangular pulses. Different symbols denote

847 peak amplitudes of 80, 120, 150 and 180 (Table 2). The dashed vertical line indicates the

848 90-ns limit.

849

850 Figure 4. The  $D_R$  and  $S_V$ : (a) all measured pulses excluding noisy and saturated ones, (b)

851 the pulses shorter than 90 ns. Black rectangles, red circles, blue upward triangles, and

852 green downward triangles represent rectangular, gaussian, ascending triangular, and

853 descending triangular pulses, respectively.

854

855 Figure 5.  $S_v^{rec}$  and  $E_{obs}^{rec}$  for the 35 short rectangular pulses whose width is 10 ns.

856

857 Figure 6.  $E_{obs}$  and  $D_R$ . The fifth polynomial equation is fitted to the data (red line).

858

859 Figure 7. Normalized transmitted laser waveform,  $\tau(t)$ .

860

861 Figure 8. Normalized transmitted laser beam pattern used for the derivation of  $E_{cal}$ .

862 The red circle on the left figure represents the field of view (FOV) of the FAR

863 telescope. The right figure shows a division image of the Ryugu surface within the FOV.

864

865 Figure 9. Examples of the calculated return pulse waveforms and the corresponding

866 footprint topographies derived from the Ryugu shape model. (Left) Transmitted time:

867 17:33:56 on 1 August 2018. The transmitted energy is 0.00151 J. Distance between the

868 spacecraft and the footprint center is 5155 m. The mean incident angle in the footprint is

869 0.204 rad. (Right) The transmitted time is 8:44:06 on 1 August 2018. The transmitted  
870 energy is 0.00133 J. Distance between the spacecraft and the footprint center is 8589 m.  
871 The mean incident angle in the footprint is 0.464 rad.

872

873 Figure10.  $E_T$  and  $D_T$ . The 3rd polynomial equation is adopted as the conversion  
874 function of the transmitted energy (thick black line). The straight blue line is previously  
875 derived by Yamada et al. (2017).

876

877 Figure 11. (a) Time variation of the albedo derived from the LIDAR data: uncorrected  
878 albedo in the top figure and corrected albedo in the bottom figure. (b) Time variation of  
879 the transmitted pulse intensity (blue points) and the temperature of the laser diode of the  
880 transmitter (red points). The data were taken on 20 July 2018.

881

882 Figure 12.  $\rho$  and incident angle for the two reflectance laws; the Lambert (blue) and the  
883 Lommel-Seeliger (orange). The 31647 data obtained on 20 July 2018 are shown for  
884 each law.

885

886 Figure 13. The map of 1.064  $\mu\text{m}$  albedo for every footprint.

887

888 Figure 14. Map of the number of footprints in each 2° by 2° grid. Without any footprint,  
889 grids are shown in white color.

890

891 Figure 15. The gridded maps of (a) 1.064  $\mu\text{m}$  albedos and (b) standard deviation in 2°  
892 by 2° grids.

893

894 Figure 16. The histogram of the albedo map shown in Figure 15a. The vertical axis is  
895 the number of bins on a log scale.

896

897

898 **Preparing tables**

Table1 The specification of the Hayabusa2 LIDAR (Mizuno et al., 2017; Yamada et al.,  
2017).

| Parameters                                    | Values  |
|---|---|
| Ranging range                                 | 30 m - 25 km (NEAR system: below 1 km, FAR system: above 1km) |
| Transmitted laser pulse energy                | $14.6 \pm 1.1$ mJ   |
| Wavelength                                    | 1.064 $\mu$ m   |
| Half the bandwidth of laser pulse             | $5.6 \pm 0.23$ ns   |
| The view angle of the FAR telescope           | 1.5 mrad  |
| Full beam divergence of the transmitter       | 2.4 mrad  |
| Area for laser receiving of the FAR telescope | 0.0095 m <sup>2</sup>   |
| Transmissivity of the optical system          | 0.678   |

|   |                           |
|---|---------------------------|
| The responsivity of the APD for<br>low level    | $50 \pm 4.5 \text{ kV/W}$ |
| The responsivity of the APD for<br>middle level | $166 \pm 28 \text{ kV/W}$ |
| The responsivity of the APD for<br>high level   | $503 \pm 83 \text{ kV/W}$ |
| Maximum data sampling                           | 1.0 Hz                    |

899

Table 2 The widths and amplitudes of pulses synthesized for the LIDAR-EM experiment.

| Pulse shape | Peak amplitude        | Full pulse width (ns)    |
|-------------|-----------------------|--------------------------|
| Rectangular | 60-240 (20 intervals) | 50                       |
|             | 80-160 (40 intervals) | 60-200 (20 ns intervals) |
|             | 200                   | 60, 80                   |

|            |                       |                               |
|------------|-----------------------|-------------------------------|
|            |                       |                               |
|            | 240                   | 60                            |
| Gaussian   | 80-200 (20 intervals) | 20-200 (20-ns intervals)      |
| Ascending  | 150, 200, 250         | 70-200 (10-ns intervals)      |
| Descending | 150                   | 70-150 (10-ns intervals)      |
|            | 200, 250              | 70-130, 150 (10-ns intervals) |

900

Table 3 The observation conditions in the selected 15 days.

| Date | Event | Altitude range (m) | Total of data |
|------|-------|--------------------|---------------|
|      |       |                    |               |

|            |   |              |       |
|------------|---|--------------|-------|
| 2018/7/20  | Science observation at<br>low altitude    | 6212 - 7832  | 36827 |
| 2018/8/1   | Science observation at<br>middle altitude | 5070 - 19946 | 84076 |
| 2018/8/6   | Gravity measurement                       | 828 - 20641  | 85625 |
| 2018/8/7   | Gravity measurement                       | 1416 - 10296 | 41291 |
| 2018/9/11  | Touchdown rehearsal                       | 1972-19943   | 72092 |
| 2018/9/20  | MINERVA release                           | 1531-19788   | 76794 |
| 2018/9/21  | MINERVA release                           | 54-15235     | 32620 |
| 2018/10/2  | MASCOT release                            | 647-19624    | 84798 |
| 2018/10/3  | MASCOT release                            | 46-2752      | 86380 |
| 2018/10/4  | MASCOT release                            | 2670-14406   | 47039 |
| 2018/10/14 | Touchdown rehearsal                       | 6206-19626   | 41971 |
| 2018/10/15 | Touchdown rehearsal                       | 21-12944     | 65334 |
| 2018/10/24 | Touchdown rehearsal                       | 952-19860    | 82719 |

---

|            |  |           |       |
|------------|--|-----------|-------|
| 2018/10/30 | Science observation at<br>low altitude | 5182-6735 | 33787 |
|------------|--|-----------|-------|

---

|            |  |           |       |
|------------|--|-----------|-------|
| 2018/10/31 | Science observation at<br>low altitude | 3134-5560 | 24726 |
|------------|--|-----------|-------|

---

901

902 Table 4 Exceptionally high and low albedo grids.

903

| Grid<br>number | Latitude | Longitude | Albedo | The standard<br>deviation of<br>albedo | Number of<br>footprints in<br>the grid | Average of<br>incident<br>angle | Deviation of<br>incident angle |
|----------------|----------|-----------|--------|--|--|---------------------------------|--------------------------------|
| 1              | -35      | 99        | 0.0720 | 0.0542                                 | 3                                      | 50.5                            | 0.772                          |
| 2              | -29      | 187       | 0.0499 | 0.0009                                 | 3                                      | 37.2                            | 0.354                          |
| 3              | -21      | 187       | 0.0510 | 0.0069                                 | 3                                      | 28.5                            | 0.825                          |
| 4              | 11       | 211       | 0.0515 | 0.0033                                 | 5                                      | 39.9                            | 2.21                           |
| 5              | -43      | 193       | 0.0292 | 0.00594                                | 8                                      | 36.1                            | 3.99                           |
| 6              | -43      | 247       | 0.0267 | 0.0010                                 | 3                                      | 50.8                            | 0.114                          |

---

|    |     |     |        |        |    |      |       |
|----|-----|-----|--------|--------|----|------|-------|
| 7  | -43 | 293 | 0.0270 | 0.0169 | 5  | 44.8 | 2.74  |
| 8  | -43 | 317 | 0.0280 | 0.0036 | 7  | 46.3 | 0.214 |
| 9  | -41 | 35  | 0.0302 | 0.0012 | 5  | 50.3 | 1.62  |
| 10 | -41 | 207 | 0.0207 | 0.0060 | 6  | 47.1 | 2.60  |
| 11 | -41 | 211 | 0.0271 | 0.0056 | 13 | 36.8 | 4.45  |
| 12 | -39 | 55  | 0.0303 | 0.0023 | 8  | 49.3 | 0.826 |
| 13 | -39 | 89  | 0.0282 | 0.0119 | 13 | 42.3 | 3.42  |
| 14 | -39 | 209 | 0.0262 | 0.0127 | 4  | 38.9 | 10.1  |
| 15 | -39 | 219 | 0.0290 | 0.0047 | 3  | 41.2 | 8.28  |
| 16 | -37 | 319 | 0.0298 | 0.0181 | 4  | 44.8 | 2.49  |
| 17 | -33 | 85  | 0.0304 | 0.0103 | 3  | 40.8 | 6.50  |
| 18 | -33 | 233 | 0.0302 | 0.0109 | 5  | 36.0 | 3.85  |
| 19 | -31 | 343 | 0.0310 | 0.0208 | 3  | 37.0 | 6.47  |
| 20 | -29 | 217 | 0.0312 | 0.0056 | 4  | 35.1 | 5.35  |
| 21 | -7  | 257 | 0.0300 | 0.0154 | 3  | 32.2 | 14.8  |
| 22 | 3   | 53  | 0.0248 | 0.0115 | 5  | 38.9 | 2.43  |

|    |    |     |        |        |     |      |       |
|----|----|-----|--------|--------|-----|------|-------|
| 23 | 3  | 325 | 0.0302 | 0.0112 | 110 | 40.6 | 8.43  |
| 24 | 5  | 107 | 0.0312 | 0.0020 | 34  | 37.6 | 1.41  |
| 25 | 7  | 73  | 0.0278 | 0.0106 | 81  | 42.5 | 3.41  |
| 26 | 7  | 75  | 0.0313 | 0.0123 | 156 | 40.3 | 4.06  |
| 27 | 7  | 155 | 0.0199 | 0.0072 | 33  | 53.8 | 8.53  |
| 28 | 11 | 99  | 0.0311 | 0.0168 | 4   | 43.6 | 7.23  |
| 29 | 15 | 327 | 0.0264 | 0.010  | 14  | 41.8 | 12.3  |
| 30 | 17 | 73  | 0.0300 | 0.0049 | 7   | 43.8 | 1.02  |
| 31 | 17 | 181 | 0.0203 | 0.0048 | 3   | 43.4 | 1.77  |
| 32 | 21 | 115 | 0.0207 | 0.0129 | 9   | 37.7 | 4.71  |
| 33 | 37 | 107 | 0.0236 | 0.0116 | 6   | 25.4 | 3.86  |
| 34 | 37 | 281 | 0.0299 | 0.0051 | 15  | 60.7 | 2.73  |
| 35 | 37 | 285 | 0.0252 | 0.0039 | 4   | 59.6 | 0.615 |
| 36 | 43 | 207 | 0.0291 | 0.0050 | 18  | 61.4 | 0.787 |
| 37 | 43 | 209 | 0.0281 | 0.0042 | 15  | 62.7 | 1.5   |



# Figures

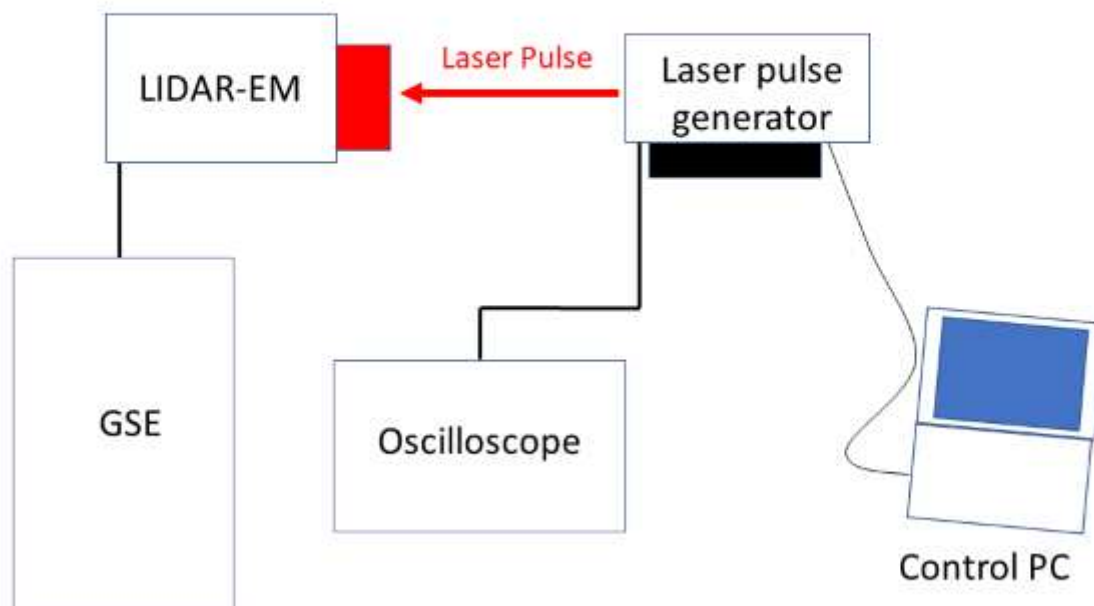


**Figure 1**

Schematic diagram of the experimental setup of the LIDAR-EM.

**Figure 2**

The examples of four types of input laser pulses in the LIDAR-EM experiment. Solid, dashed, dotted, and dash-dotted lines indicate rectangular, gaussian, ascending triangular, and descending triangular pulses, respectively. Widths and peak amplitudes are 60 ns and 120, 40 ns and 120, 70 ns and 150, and 70 ns and 150, respectively. The horizontal thick dashed line indicates the noise floor of the records.

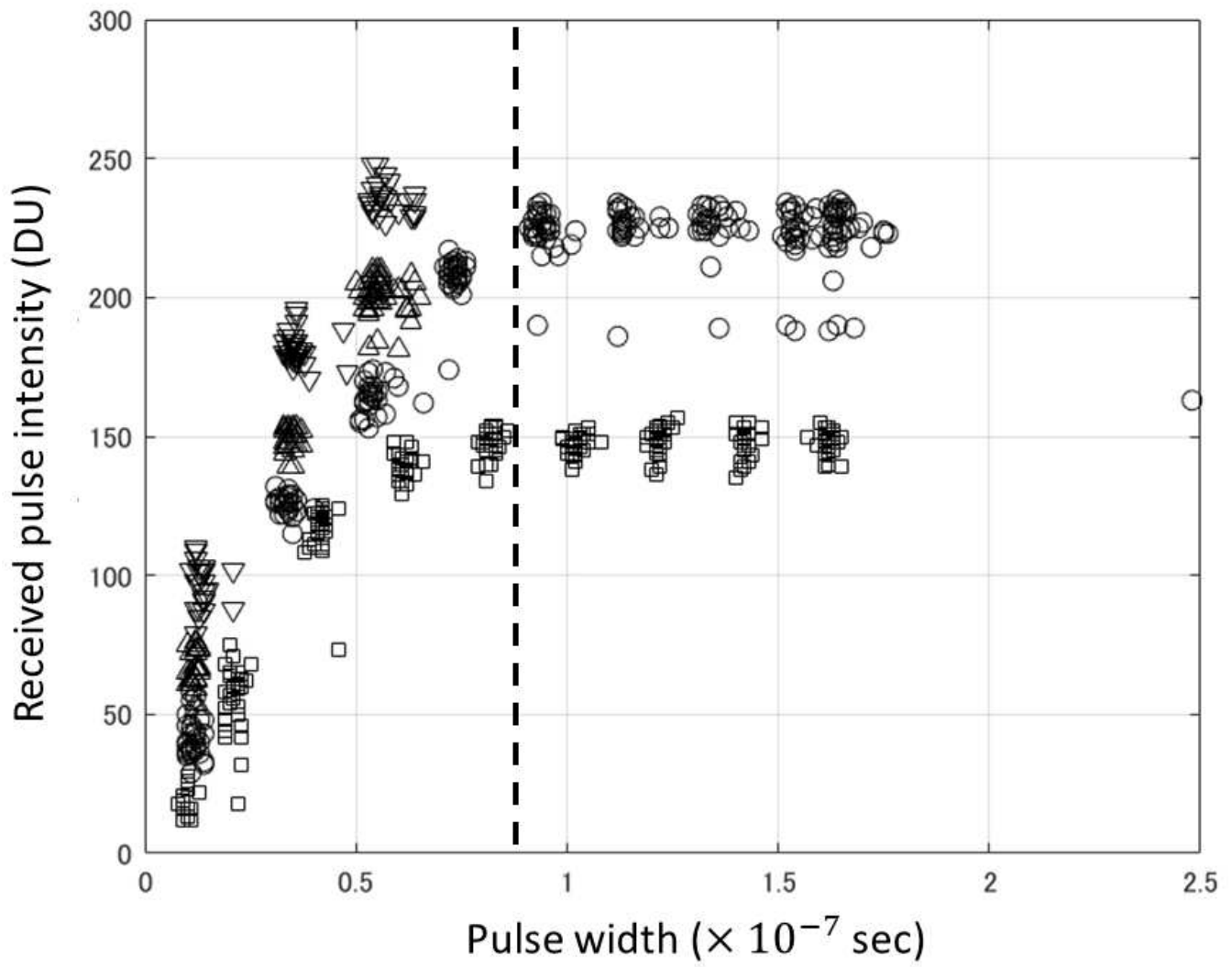


**Figure 3**

The pulse width and  $D_R$  for the rectangular pulses. Different symbols denote peak amplitudes of 80, 120, 150 and 180 (Table 2). The dashed vertical line indicates the 90-ns limit.

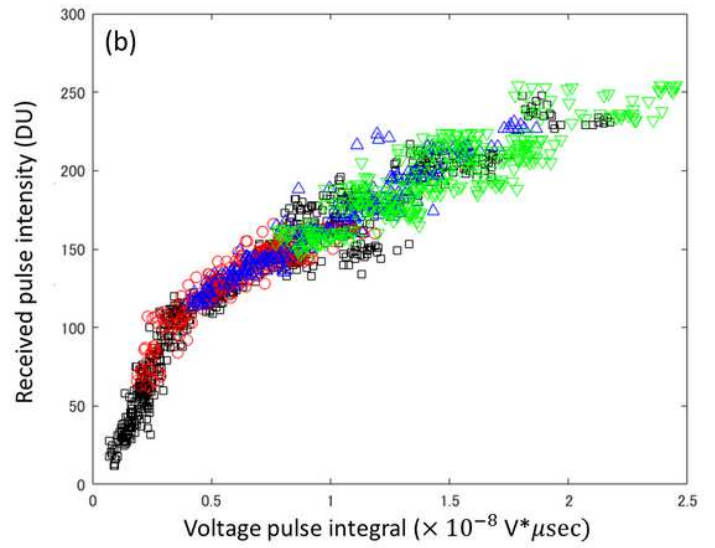
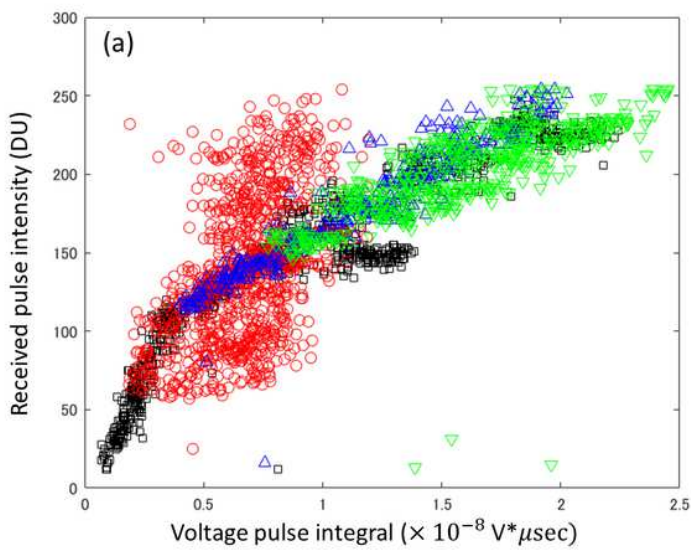


**Figure 4**

The  $D_R$  and  $S_V$ : (a) all measured pulses excluding noisy and saturated ones, (b) the pulses shorter than 90 ns. Black rectangles, red circles, blue upward triangles, and green downward triangles represent rectangular, gaussian, ascending triangular, and descending triangular pulses, respectively.

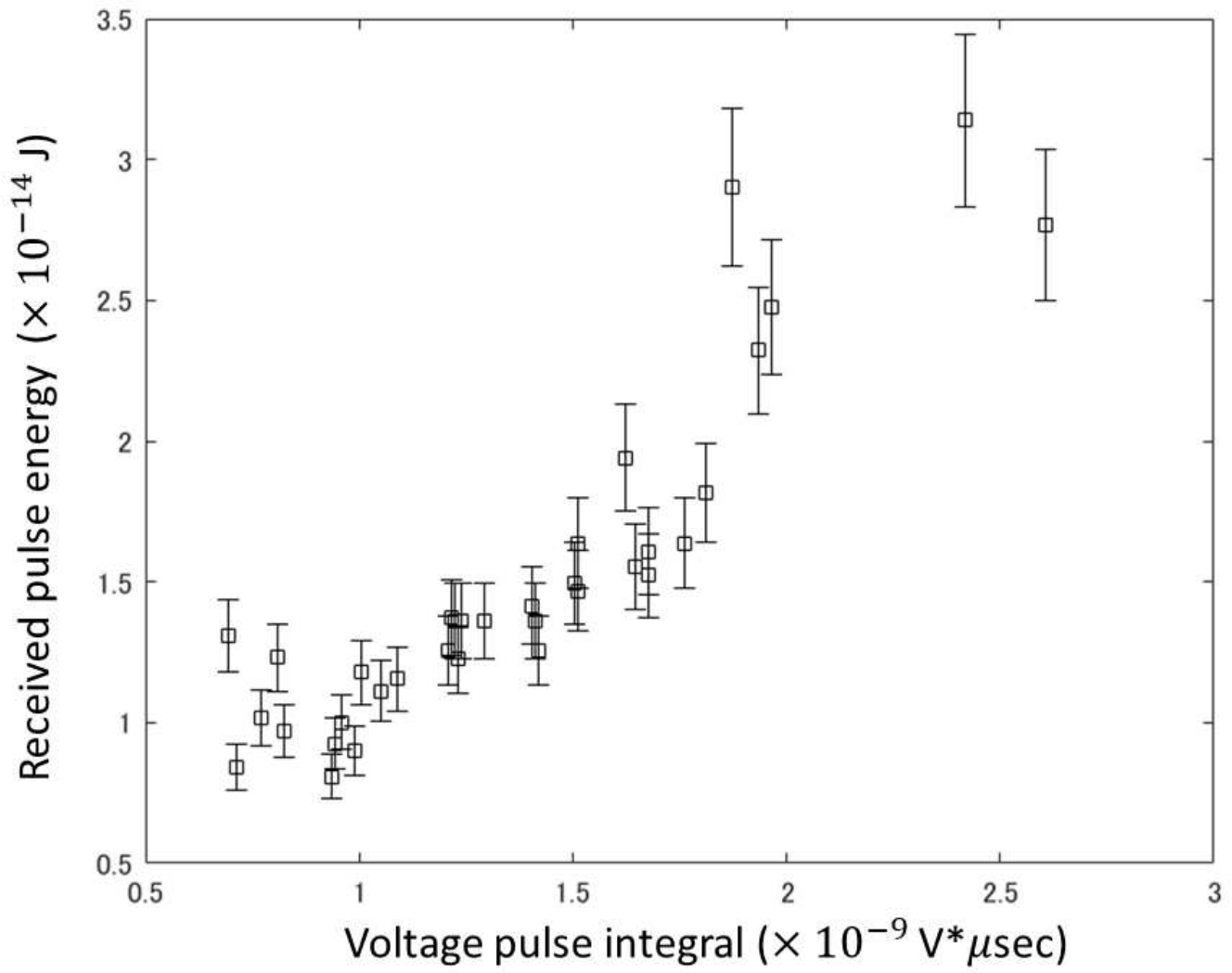


Figure 5

$S_V^{rec}$  and  $E_{obs}^{rec}$  for the 35 short rectangular pulses whose width is 10 ns.

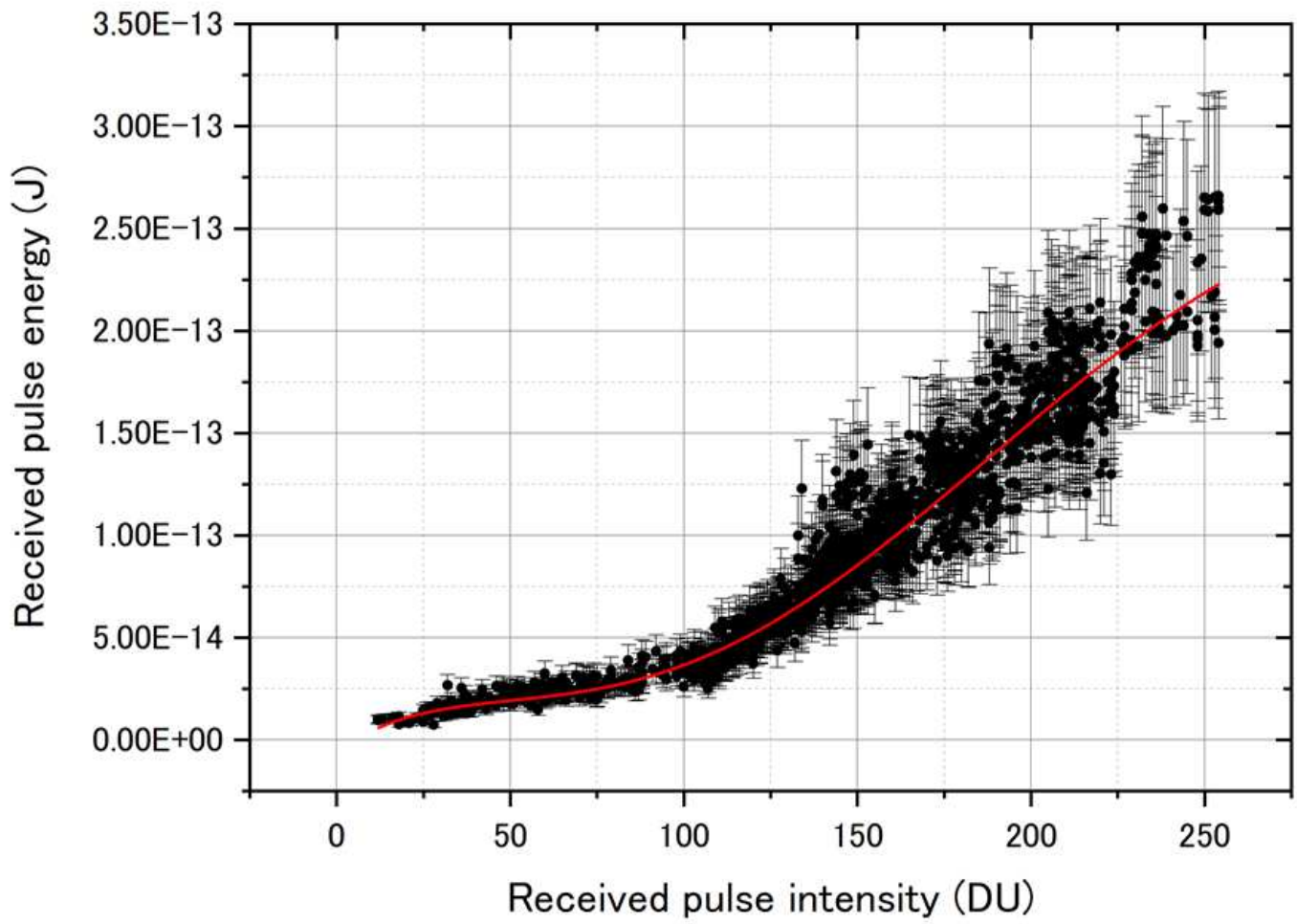
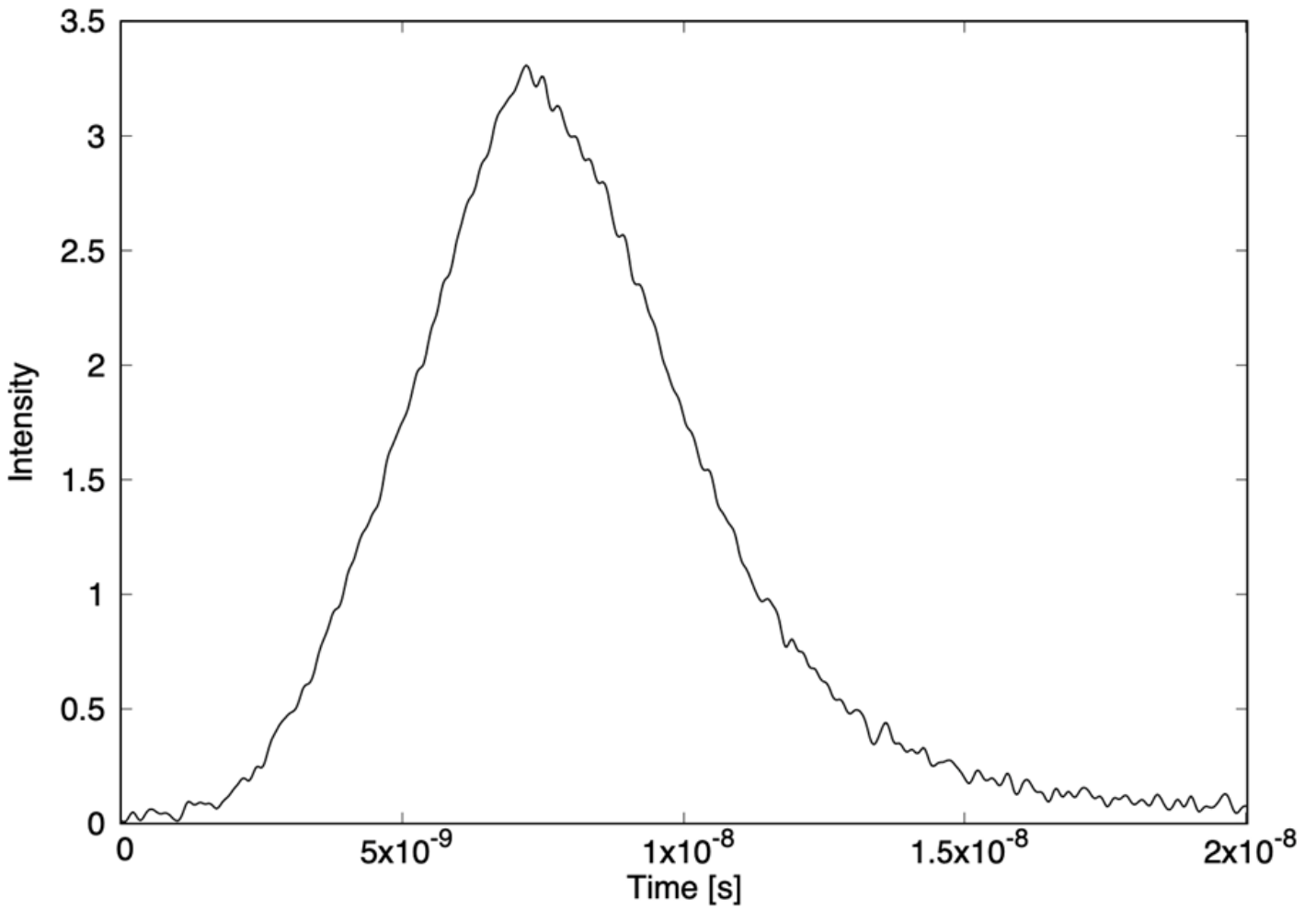


Figure 6

$S_{obs}$  and  $D_R$ . The fifth polynomial equation is fitted to the data (red line).



**Figure 7**

Normalized transmitted laser waveform,  $\tau(t)$ .

**Figure 8**

Normalized transmitted laser beam pattern used for the derivation of  $E_{\text{cal}}$ . The red circle on the left figure represents the field of view (FOV) of the FAR telescope. The right figure shows a division image of the Ryugu surface within the FOV.

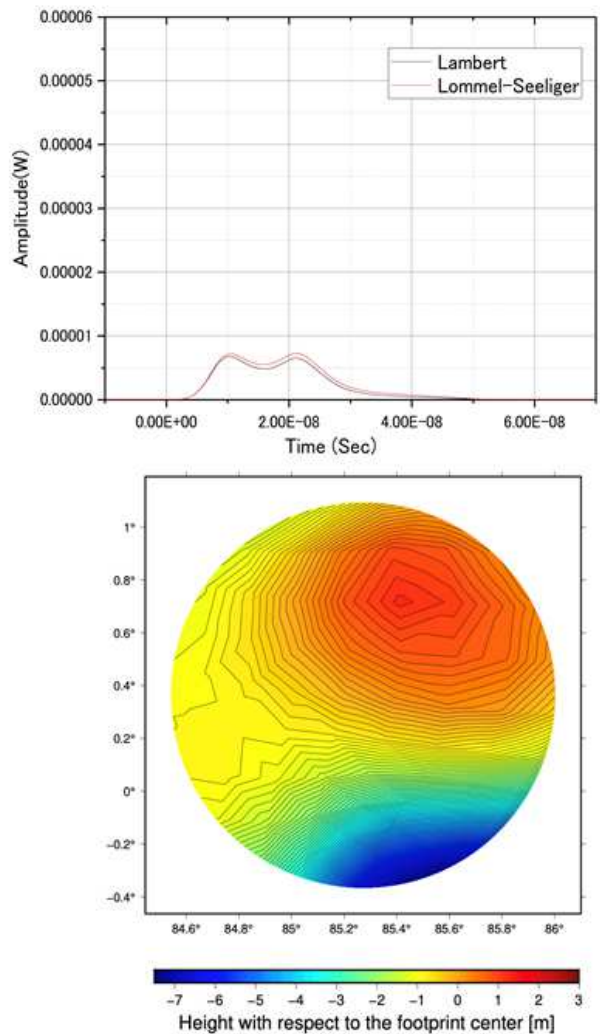
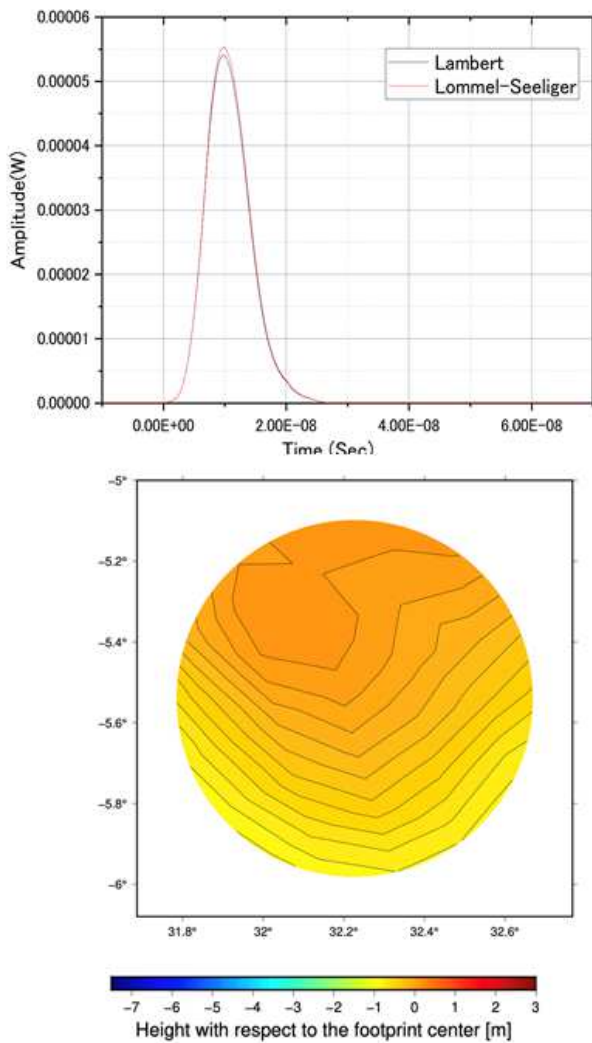


**Figure 9**

Examples of the calculated return pulse waveforms and the corresponding footprint topographies derived from the Ryugu shape model. (Left) Transmitted time: 17:33:56 on 1 August 2018. The transmitted energy is 0.00151 J. Distance between the spacecraft and the footprint center is 5155 m. The mean incident angle in the footprint is 0.204 rad. (Right) The transmitted time is 8:44:06 on 1 August 2018. The transmitted energy is 0.00133 J. Distance between the spacecraft and the footprint center is 8589 m. The mean incident angle in the footprint is 0.464 rad.

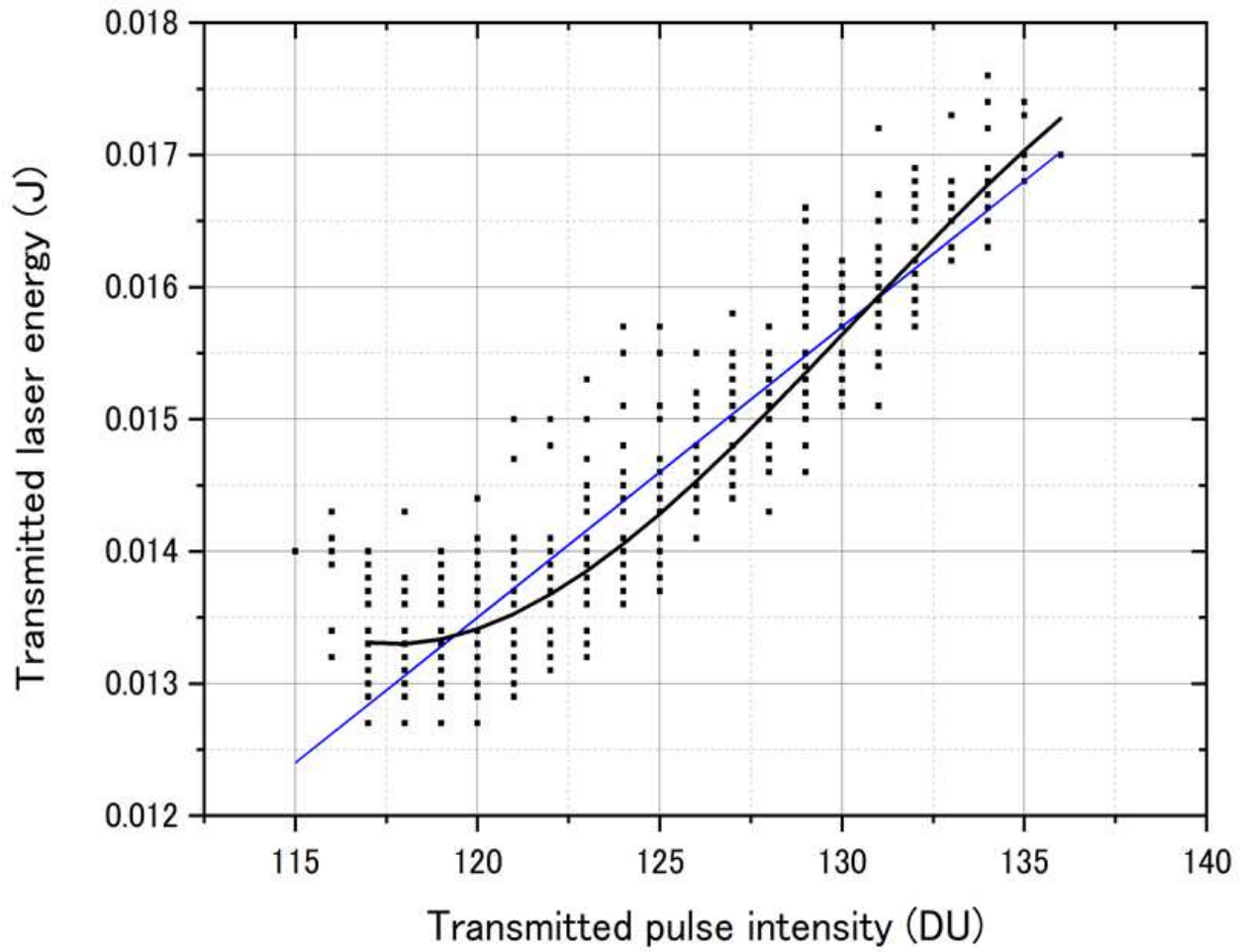


**Figure 10**

$E_T$  and  $D_T$ . The 3rd polynomial equation is adopted as the conversion function of the transmitted energy (thick black line). The straight blue line is previously derived by Yamada et al. (2017).

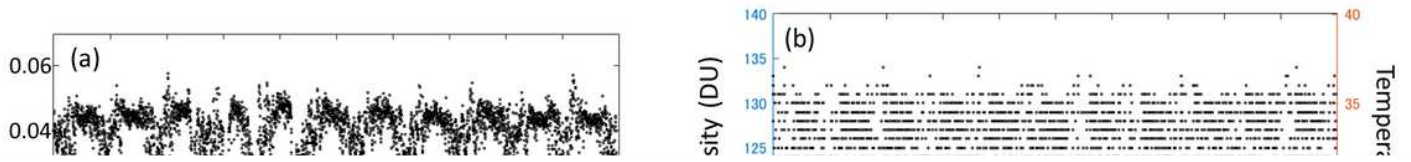


**Figure 11**

(a) Time variation of the albedo derived from the LIDAR data: uncorrected albedo in the top figure and corrected albedo in the bottom figure. (b) Time variation of the transmitted pulse intensity (blue points) and the temperature of the laser diode of the transmitter (red points). The data were taken on 20 July 2018.

**Figure 12**

$r$  and incident angle for the two reflectance laws; the Lambert (blue) and the Lommel-Seeliger (orange). The 31647 data obtained on 20 July 2018 are shown for each law.

**Figure 13**

The map of  $1.064 \mu\text{m}$  albedo for every footprint.

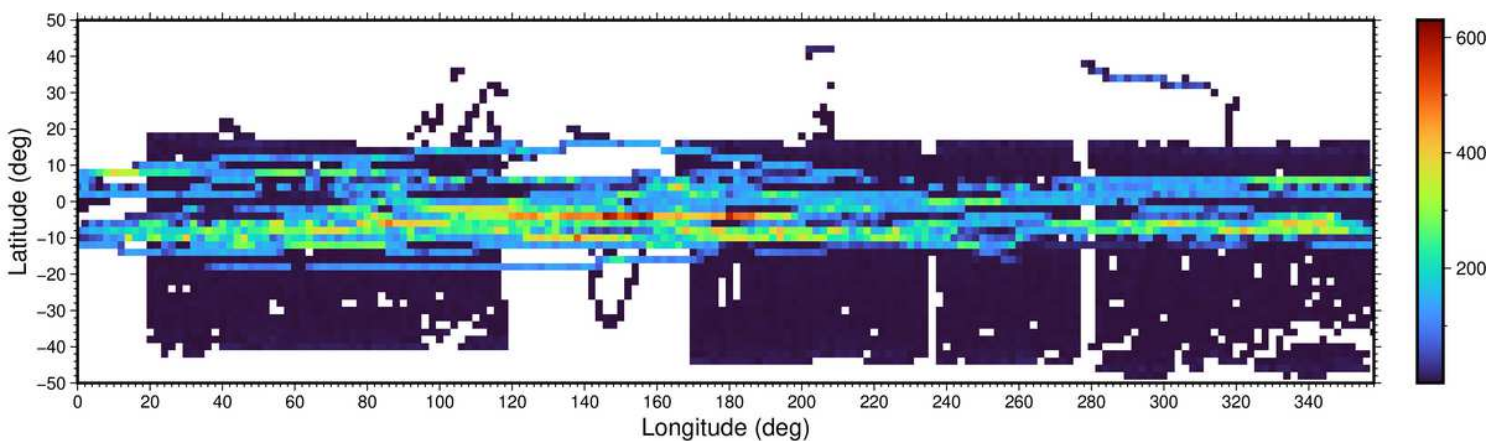
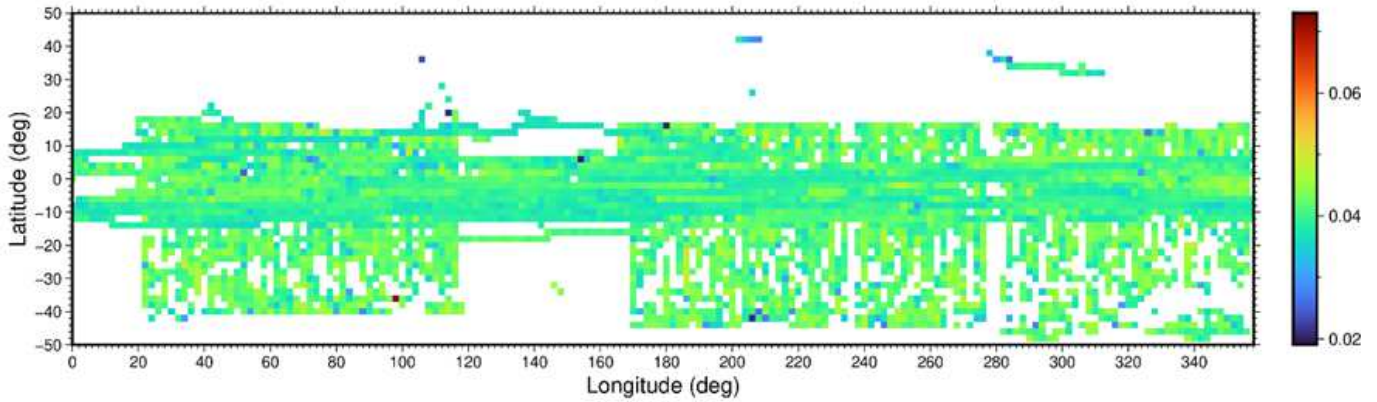
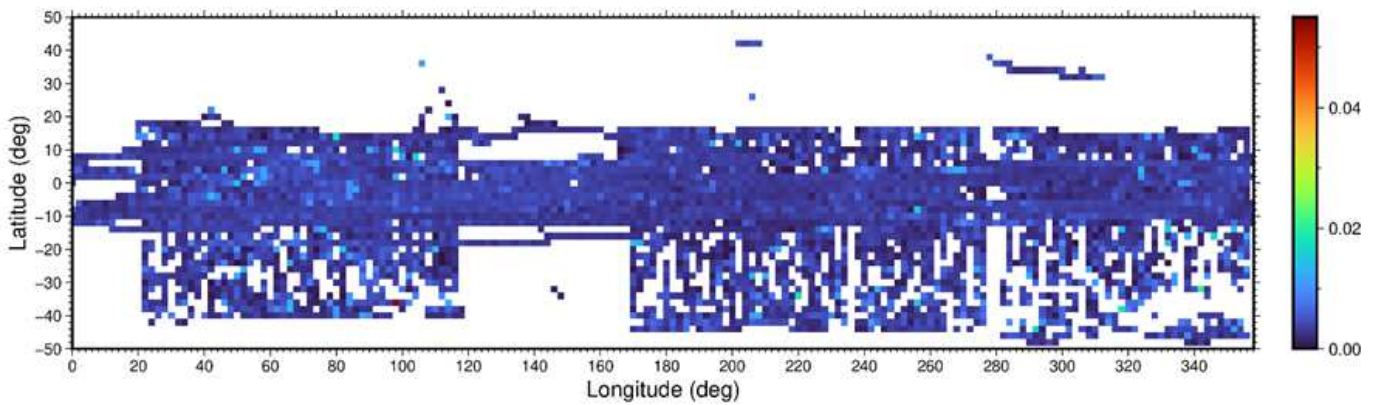


**Figure 14**

Map of the number of footprints in each 2° by 2° grid. Without any footprint, grids are shown in white color.



(a)



(b)

**Figure 15**

The gridded maps of (a) 1.064  $\mu\text{m}$  albedos and (b) standard deviation in 2° by 2° grids.

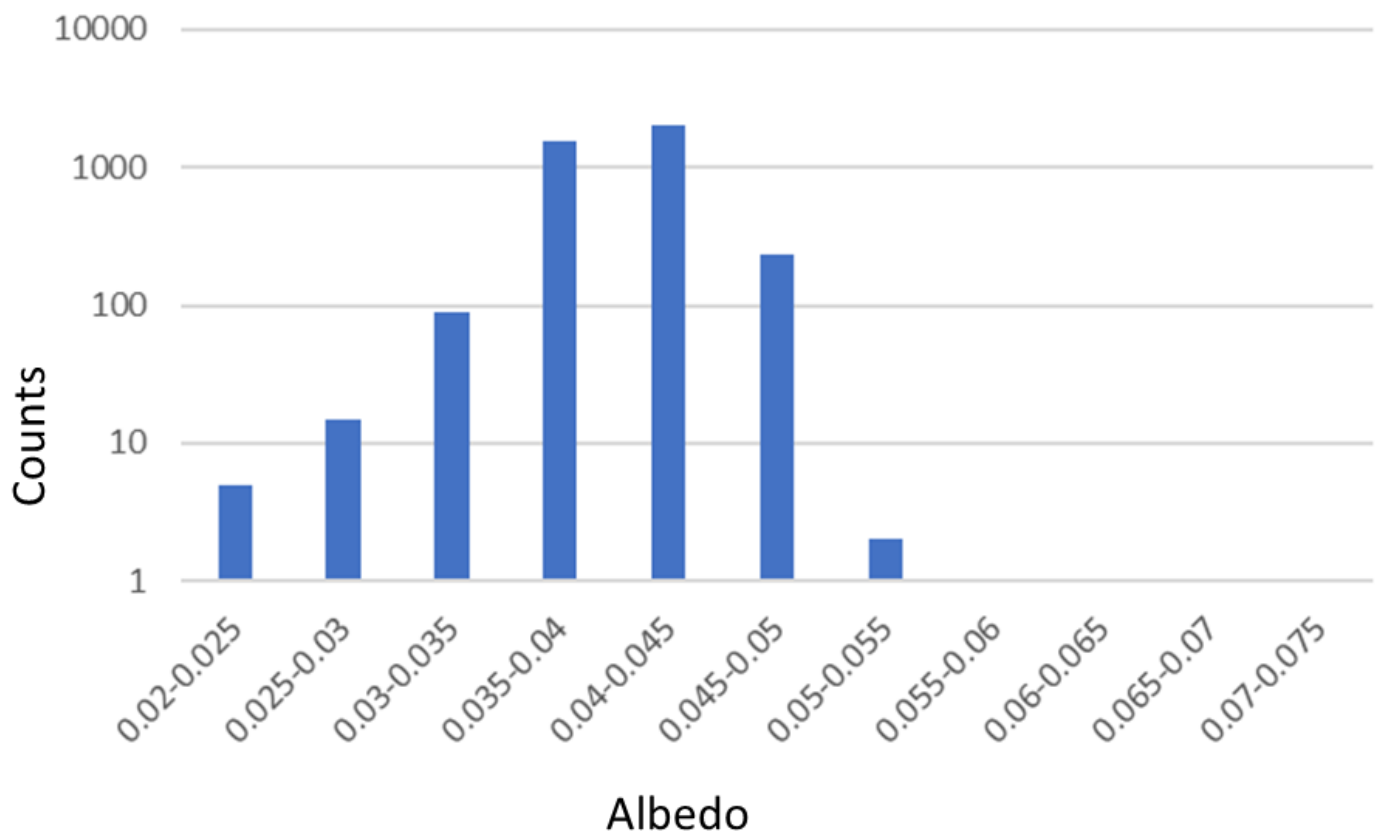


**Figure 16**

The histogram of the albedo map shown in Figure 15a. The vertical axis is the number of bins on a log scale.

## Supplementary Files

This is a list of supplementary files associated with this preprint. Click to download.

- [Graphicalabstractsubmitt.jpg](#)